Optical propagation within a three-dimensional shadowed atmosphere–ocean field: application to large deployment structures

John P. Doyle and Giuseppe Zibordi

Estimation of optical shadowing effects that occur on *in situ* submerged radiance and irradiance measurements conducted in the proximity of a large and complex three-dimensional deployment structure is addressed by use of Monte Carlo simulations. We have applied backward Monte Carlo techniques and variance reduction schemes in three-dimensional radiative transfer computations of in-water light field perturbations by taking into account relevant geometric, environmental, and optical parameters that describe a realistic atmosphere–ocean system. Significant parameters, determined by a sensitivity analysis study, have then been systematically varied for the computation of an extensive set of correction factors, included in look-up tables designed for operational removal of tower-shading uncertainties, which typically induce an ~1–10% decrease in absolute radiometric data values near a specific oceanographic tower located in the northern Adriatic Sea. In principle, the proposed correction methodology can be transferred to other deployment systems, instrument casings, and measurement sites if a comprehensive description is provided for the system parameters and their variability.

OCIS codes: 010.1290, 010.4450, 030.5620.

1. Introduction

The presence of a finite deployment structure close to an optical measurement point introduces abrupt medium changes, breaks the translation-invariant symmetry within a plane-parallel atmosphere–ocean system, and casts shadow perturbations on the surrounding radiant energy field, all of which produce light field inhomogeneities in all three spatial dimensions.

Studies by several authors[1–7] have addressed uncertainties induced in underwater optical measurements by large structures such as ships or oceanographic towers, whereas minimum deployment distances of optical instruments operated from ships have been empirically estimated by Mueller and Austin.[8] However, no operational correction methodology—based on quantitative estimations—has yet been developed to remove shadowing uncertainties caused by these large deployment structures on the in-water optical measurements. The three-dimensional (3-D) structure of different deployment platforms can vary considerably. This hinders the formulation of a general correction scheme that is capable of providing the highly accurate radiometric quantities required in bio-optical modeling, validation of optical remote-sensing products, and vicarious calibration of optical space sensors.

Shadowing radiance L and irradiance E fields in the proximity of light-obstructing structures (e.g., deployment towers, moored buoys, instrument casings) is an inherently 3-D problem, which can be effectively addressed and reproduced by Monte Carlo (MC) simulation.[1,9] The 3-D backward MC modeling of radiative transfer processes in the Sun–atmosphere–ocean-structure–detector system can ensure efficient simulation of the L and E fields, producing a lower variance than that obtained by forward MC modeling. In particular, correlated photon tracking techniques,[10] elaborated and implemented in the recently developed PHO-TRAN MC code,[11,12] have shown their ability to estimate the

J. P. Doyle (j.doyle@ic.ac.uk) is with the Department of Computational Physics and Geophysics, T. H. Huxley School, Imperial College of Science, Technology, and Medicine, University of London, London SW7 2BP, UK. G. Zibordi (giuseppe.zibordi@jrc.it) is with the Marine Environment Unit, Space Applications Institute, Joint Research Centre of the European Commission, I-21020 Ispra (Va), Italy.

Received 16 August 2001; revised manuscript received 14 January 2002.

0003-6935/02/214283-24$15.00/0

shadowing perturbation effects that appear in optical measurements.

The purpose of this research is to illustrate the development of a reliable and accurate methodology established to correct for shadowing perturbations induced on in-water radiance and irradiance measurements, as taken close to the *Acqua Alta* Oceanographic Tower (AAOT) located in the northern Adriatic Sea and used to support ocean color validation activities. The proposed correction scheme is based on low-variance backward MC simulations of in-water radiometric measurements. The computation scheme has been validated with published data, whereas the correction scheme has been perfected on the quantitative findings from a sensitivity analysis study.

2. Monte Carlo Simulations

MC methods, when applied to visible and near-infrared radiative transfer problems, provide the photon intensity and directional fields (e.g., the L distribution) at any given virtual measurement point. One can achieve this by properly initiating, tracking, and tallying an adequate number of photons emitted from the source that reach the detector after random walk propagation,[13] rather than by formal solution of the associated radiative transfer equation (RTE). MC methods allow for a completely 3-D geometry description of the media embedded in the simulated system and can take into account detailed radiation–matter interactions, without the mathematical load usually needed by other computational approaches based on formal solution of the RTE. The tracking of photons is obtained by accurate simulation of particlelike transport and collision events that occur across the system and is governed by stochastic application of the physics that describes these events. We tally photons by counting their contributions to the signal at the detector point and categorize them according to their properties, direction, and tracked history. Estimates of mean detector responses (e.g., L and E measurements) and of their variances are then statistically obtained.

The physics that describes the spectrally dependent radiation–matter interactions that are included in the PHO-TRAN MC model of radiative transfer—as occurs in the visible and near-infrared energy range, across a coupled atmosphere–ocean realistic system and in the presence of shadow-casting totally absorbing structures—are photon absorption by molecules, by particles, and on dielectric interfaces; multiple scattering from small scattering centers (molecular Rayleigh scattering in air, density fluctuation scattering in water) and from larger scattering centers (Mie particle scattering); bidirectional reflection from dielectric interfaces (although simple Lambertian reflection is assumed here); Snell's refraction and Fresnel's reflection (including total internal reflection) at the interface between media with different refractive indices. The air–sea reflecting and transmitting interface is statistically described, within the general version of the PHO-TRAN MC code, by allowance for the wind-roughened capillary waves described by a Cox–Munk sea surface slope distribution function,[14] although the sea surface is assumed flat for the scope of this investigation.

Within the PHO-TRAN MC simulations, the atmosphere–ocean system is modeled on a 3-D reference frame with a right-handed Cartesian set of orthogonal axes, on which we placed a grid that describes the geometric features of the problem. The grid defines macroscopic volumes (cells) that contain media of homogeneous optical properties. Simple cell volumes are 3-D boxes having vertices defined by grid points. The code can handle quadratic surface geometry, which allows more complex structures to be defined (e.g., spheres and cylinders). In each cell of the grid, where a mixture of materials is allowed for, the optically significant components (OSCs) are specified and their spectral inherent optical properties (IOPs) are assigned. The OSCs included in the simulations are air molecules, aerosols, pure seawater, and hydrosols. The latter are defined here and throughout the rest of the paper to describe collectively, from an optical standpoint, the in-water suspended particles and dissolved matter of both organic and inorganic nature (i.e., the in-water components different from pure seawater). Each OSC is described by its IOPs: beam attenuation coefficient c_{OSC} ($\equiv a_{\mathrm{OSC}} + b_{\mathrm{OSC}}$), single-scattering albedo ω_{OSC} ($\equiv b_{\mathrm{OSC}}/c_{\mathrm{OSC}}$), and scattering phase function P_{OSC}, where a_{OSC} and b_{OSC} are the absorption and scattering coefficients, respectively, and b_{OSC} is related to P_{OSC} through the volume-scattering function $\beta_{\mathrm{OSC}} = b_{\mathrm{OSC}} P_{\mathrm{OSC}}$ (the scattering angle dependency of both P_{OSC} and β_{OSC} is omitted for brevity). Moreover, b_{OSC} is defined by integration of β_{OSC} over all solid angle elements $d\Omega$ from the scattering center (or, if assuming azimuthally symmetric phase functions, over all annular elements $2\pi \sin\psi\, d\psi$ at polar scattering angle ψ taken from the forward-scattering direction), giving $b_{\mathrm{OSC}} = \int \beta_{\mathrm{OSC}}\, d\Omega = 2\pi \int_0^{\pi} \beta_{\mathrm{OSC}} \sin\psi\, d\psi$. A combination of the former and the latter equations gives the normalization condition for the phase function $2\pi \int_0^{\pi} P_{\mathrm{OSC}} \sin\psi\, d\psi = 1$. Each cell that contains a mixture of materials exhibits total IOPs (c_{tot}, ω_{tot}, and P_{tot}) obtained as a coherent and weighted sum of individual IOPs. Specifically, for a cell that contains N different j-indexed OSC_js, the total IOPs are obtained as $c_{\mathrm{tot}} = \Sigma c_{\mathrm{OSC}_j}$, $\omega_{\mathrm{tot}} = b_{\mathrm{tot}}/c_{\mathrm{tot}} \equiv b_{\mathrm{tot}}/(a_{\mathrm{tot}} + b_{\mathrm{tot}})$, and $P_{\mathrm{tot}} = \beta_{\mathrm{tot}}/b_{\mathrm{tot}}$, where $a_{\mathrm{tot}} = \Sigma a_{\mathrm{OSC}_j}$, $b_{\mathrm{tot}} = \Sigma b_{\mathrm{OSC}_j}$, $\beta_{\mathrm{tot}} = \Sigma b_{\mathrm{OSC}_j} P_{\mathrm{OSC}_j}$, and the sums are extended over index j to all the N OSC_js contained in the cell. The refractive index n of the mixture contained in the cell is specified. In particular, the air and seawater refractive indices are assigned: n_{atm} for the atmosphere and n_{oce} for the ocean.

Cell boundaries (i.e., interfaces between cells and with outer space) are spectrally characterized by transmittance and reflectance and by the associated transmission and reflection angular distribution functions (ADFs), which could be bidirectional in

character. Specific ADFs are also defined for the source angular emission and for the detector angular collection response. Atmospheric and oceanic layers and their boundaries [top of the atmosphere (TOA), sea surface, and sea floor] are generally horizontally plane–parallel, except those layers in which a geometric object that schematically represents a portion of the shadowing structure is introduced at a specific location within the 3-D reference frame. The shadowing structure and its surfaces are assumed to be totally absorbing for all practical purposes, i.e., $\omega_{tot} = 0$. Overcast sky conditions are simulated as a special case by allowing for a uniform above-water incident radiance distribution, i.e., directional density of incident photons is proportional to the cosine of the incident zenith angle.

The solar source is described by a parallel beam of monochromatic photons that originate from a far-field point, and uniformly impinge on the TOA. The emission directional distribution for the source is therefore formulated by means of a Dirac δ centered on solar zenith θ_0 and solar azimuth ϕ_0. The θ_0 angle and its cosine μ_0 are considered to be positive from the vertically upward direction, whereas ϕ_0 is considered to be clockwise from the northbound meridian.

The detectors are described by their geometric location, their field of view (FOV), and their ADF for the accepted incoming photons. For simulated radiances the FOV is a Dirac δ or a 20° FOV cone as per in-water field radiometer specifications, whereas for irradiances it is a 2π sr solid angle. Upwelling (downwelling) radiances and irradiances present an ADF centered on the vertically down (up) direction. For irradiances (only plane irradiances are considered here), the distribution of detected directions follows the typical cosine-collector law, so the ADF is the cosine of the angle of acceptance with respect to the normal to the irradiance detector plane, across the full hemispheric FOV.

The tracked photon (assumed monochromatic, with no energy redistribution processes, such as fluorescence or Raman scattering, accounted for) is essentially described by a set of six parameters: position ($X = x, y, z$), flight direction ($\Theta = \theta, \phi$), and statistical weight (W). The polar angle of flight θ and its cosine μ are considered positive from the upward z axis, whereas the azimuth angle of flight ϕ increases counterclockwise from the positive x axis. The photon has other parameters (actually counters) associated with it, such as number of undergone collisions, absorption and scattering events, and reflection–transmission interfaces that categorize its history.

A. Backward Monte Carlo

Photons detected by a radiometer are a fraction of those emitted by the Sun and reach the sensor after absorption, scattering, reflection, refraction, and transport processes within the atmosphere–ocean system. The properties of physical processes that characterize the propagation of photons are time reversal invariant; hence the inverse course of events can be applied by simulations. This principle is the basis for the backward MC technique. Here backward MC algorithms have been developed based on Case's reciprocity relationship[15] and on Gordon's implementations.[1] Random walk photon trajectory sampling is performed the same way in backward MC simulations as in forward MC simulations, but contributions to the detected signal are deterministically computed to ensure high computational efficiency.[1]

Different from forward MC, in the backward MC scheme photons with initial unitary statistical weight W_0 are released from the detector within its FOV according to the predefined collection ADF. The forward MC detector therefore becomes a source in the backward MC scheme, whereas the forward MC solar source is a point detector in the backward MC scheme and is treated as if located at an infinite distance from the simulated atmosphere–ocean system. After the photon emission from the detector, a free-flight optical distance τ_p to the next collision point is sampled,[16] possible cell-boundary crossing processes are considered to define flight direction modifications, and, finally, photon trajectory is computed when we take into account possible changes in IOPs along the propagated optical path.

At the collision point, defined as the point at which the sampled optical distance is exhausted, a scatterer (i.e., a specific OSC) is sampled, then the photon survival probability ω_{tot} is computed, and the flight direction of the absorption-surviving photon is determined by retrieval of the scattering angle from a random sampling of an azimuthally symmetric P_{OSC}. The latter is adequately modeled into an equal-probability interval table.[16]

The probability of a backtracked photon to propagate randomly toward the Sun is virtually zero. Therefore, at collision and boundary crossing points, photon contributions to the detected signal are deterministically computed. We did this by calculating the probability that a photon scatters in directions leading to the Sun and by evaluating the associated weight reduction given by the attenuation along the traveled path and by the possible absorption at the interface transmission. If this virtual photon encounters a purely absorbing medium (e.g., the tower structure), its contribution to the detected signal is zero.

B. Photon Backward Tracking

A simulation recipe is given here as an analytical breakdown of the backward MC algorithms. In the following, an event is defined either by a photon emission, a collision (leading to absorption or scattering), or a capture by the detector.

1. First Event

Reverse-propagating photons of initial unitary weight ($W_0 = 1$) are released from the detector point in the antiparallel direction of physical propagation that characterizes the original forward-traveling photon on its way to detection. The direction of

backward emission is chosen according to the detector's ADF. For downwelled irradiance E_d, the emission direction of the backward photon is chosen so that the cosine μ_p of the polar angle θ_p that identifies the backward photon direction with respect to the upward normal to the horizontal detector plane is randomly but uniformly distributed between 0 and +1 (between 0 and −1 for upwelled irradiance, E_u). We operated this random choice by sampling from the 3-D hemispheric cosine directional distribution. This distribution is defined by a probability density function (PDF) given by $p_{\cos}(\mu_p) = 2\mu_p$, analytically providing a cumulative distribution function (CDF) equal to $C_{\cos}(\mu_p) = {\mu_p}^2$. The latter is associated with a random number u, uniformly distributed in the 0–1 interval and sampled therefrom—briefly $u \in U[0, 1]$—and thereby giving a sampled $\mu_p = \sqrt{u}$. The azimuth angle ϕ_p of the emitted direction is determined by another random number u (the same symbol is used here for simplicity) uniformly distributed between 0 (not inclusive) and 2π rad, i.e., $u \in U(0, 2\pi]$ rad. For nadir upwelled radiance L_u, the emission direction is invariably chosen as downward ($\mu_p = -1$; $\phi_p = 0$) or randomly within a 20° FOV cone when field radiometers are simulated. This emission constitutes the first event in the life history of the backtracked photon's trajectory, and it provides an initial photon flight direction to which a sequence of random walk trajectories is subsequently added, collectively providing an important part of the so-called photon history.

2. *Second and Further Events*

Having determined an emission direction, a free-flight distance to the next collision point is computed *a priori* by randomly sampling an optical path length τ_p from the exponential distribution [with the PDF given by $p_{\exp}(\tau_p) = \exp(-\tau_p)$, from which a CDF is analytically obtained as $C_{\exp}(\tau_p) = 1 - \exp(-\tau_p)$, related to a random number $u \in U[0, 1]$, thereby giving a sampled $\tau_p = -\ln u$]. The corresponding geometric distance ξ is computed according to the local IOP values encountered along the propagated optical path ($\xi = \Sigma \tau_{p_j}/c_j$, where the sum is extended to all $j = 1, \ldots, M$ photon-traveled cells, each with beam attenuation c_j, and in each of which an optical distance τ_{p_j} has been exhausted, where $\tau_p - \Sigma_1^{j-1} \tau_{p_i} \leq \tau_{p_j} \leq \tau_p$ and the sum is extended to the running index $i = 1, \ldots, j - 1$). The parameter τ_p is included in the set of parameters that characterize the photon properties.

If the free flight is interrupted by an intercell boundary crossing through the 3-D mesh, the properties of the interface and of the two media that fill the cells are considered. If the boundary crossing implies a change in the associated medium's IOPs, and/or a boundary transmission–reflection directional redistribution function is active at the interface (from here onward referred to as significant boundary crossing), computations account for the remaining free-flight distance as well as the possible absorption at the interface and the possible change in flight direction as could result, for example, from a change in refractive index through the crossed media. In this case, Fresnel reflectivity ρ_r and transmittivity ρ_t coefficients are computed, the transmitted and reflected directions are assigned from geometrical-optics computations (allowing for total internal reflection), and we chose the actual direction by sampling a random number $u \in U[0, 1]$. If $u < \rho_r$, a reflection occurs; otherwise, a transmission takes place. Finally, the corresponding Fresnel coefficient multiplies the photon's weight, which, if transmitted, is then multiplied by the so-called Straubel invariant.[17] This factor, ${n_{\text{oce}}}^2/{n_{\text{atm}}}^2$, is for photons incident at the sea surface from the atmosphere (the inverse factor applies to photons incident at the sea surface from the sea) and is induced by refraction. This invariant factor causes an above-surface small solid angle to be focused into a narrower solid angle below the surface (and vice versa) and thus amplifies the in-water photon flux per given solid angle. In case of reflection from a Lambertian surface, the photon weight is multiplied by its survival probability (the Lambertian surface reflectance coefficient r_b), and the cosine μ_r of the polar angle θ_r of reflection with respect to the outward normal to the surface is computed similarly to μ_p as derived previously for irradiance emission. The Lambertian reflection polar angle PDF is $p_{\text{Lam}}(\mu_r) = 2\mu_r$. Its CDF is therefore $C_{\text{Lam}}(\mu_r) = {\mu_r}^2$, which is related to $u \in U[0, 1]$, thus giving $\mu_r = \sqrt{u}$. The azimuth angle ϕ_r of the Lambertian reflected direction is determined by another random number $u \in U(0, 2\pi]$ rad.

Each of the previously described significant boundary crossings constitutes an additional event in the photon's history. If the boundary crossing occurs with no IOP change or no activation of a specific interface redistribution function takes place, the crossing is insignificant and constitutes a pseudo-event of no influence to the photon's trajectory and weight.

At the computed collision point an absorption event, or one of the possible scattering events, is sampled (as occurs on molecules or on particles) according to the following criteria. A random number $u \in U[0, 1]$ is compared with the local value η_c of the ratio of the total scattering to the total beam attenuation coefficient (i.e., $\eta_c \equiv \omega_{\text{tot}}$) to determine if scattering ($u < \eta_c$) or absorption occurs. If an absorption event occurs, the photon is removed from the MC game and a new photon is ejected from the detector. In general, a variance reduction technique, i.e., forced absorption, is devised to avoid this, as detailed in Appendix A, unless $\omega_{\text{tot}} = 0$. If one of the possible scattering events occurs, a random number $u \in U[0,1]$ is compared with the local value η_b of the ratio of the molecular to total scattering coefficient to determine upon which OSC scattering will take place. If $u < \eta_b$, the scattering event is a molecular type (Rayleigh or density fluctuation, respectively, in the atmosphere or in the ocean), otherwise it is due to a particle (aerosol or hydrosol, respectively, in the atmosphere or in the ocean).

The new direction of scattered flight is sampled from the OSC-associated scattering phase function P_{OSC} according to the following scheme. The azimuthal scattering angle ϕ_s, which defines the rotation of the scattering plane, is determined by a random number $u \in U(0, 2\pi]$ rad. The polar scattering angle ψ, which defines the angle between directions prior to and after collision, is determined by another random number $u \in U[0, 1]$, which is compared to the CDF of the scattering process. This comparison is made on the CDF equal probability intervals[16] because the scattering PDF, $p_{\mathrm{OSC}}(\psi)$, does not allow for the analytic inversion method. This method is instead applicable to the previously described distributions associated with PDFs $p_{\cos}(\mu_p)$, $p_{\exp}(\tau_p)$, and $p_{\mathrm{Lam}}(\mu_r)$. The CDF for scattering, $C_{\mathrm{OSC}}(\psi)$, is the progressive integral of $p_{\mathrm{OSC}}(\psi)$, which is given by the corresponding scattering phase function $P_{\mathrm{osc}}(\psi)$ multiplied by a $2\pi \sin\psi$ factor to allow for all the scattering that occurs within a solid angle annular element (assuming that the phase functions are azimuthally symmetric): $C_{\mathrm{OSC}}(\psi) = 2\pi \int_0^{\psi} P_{\mathrm{OSC}}(\psi')\sin\psi' \, d\psi'$. The integration over ψ' is performed numerically, and equal probability intervals are obtained within the full $[0, \pi]$ rad domain by construction of appropriate sequences of ψ values, which we determined by imposing each interval to subtend an equal area under the $C_{\mathrm{OSC}}(\psi)$ curve. Typically, 1000 intervals are considered—cumulatively subtending a unitary area across the full ψ domain, since the PDF is normalized to unity—and are directly associated with the sampled $u \in U[0, 1]$.

A collision followed by scattering implies that a new τ_p must be sampled, that the photon will initially travel along the scattered direction, and that a further event in the photon's history will occur at a different point in the atmosphere–ocean system unless the photon escapes from the simulated system. In general, a variance-reduction technique, i.e., forced collisions, is devised to avoid this situation as detailed in Appendix A.

3. *Deterministic Contributions*

The probability of a backtracked photon to travel aligned with the extraterrestrial solar flux and to propagate successfully into the Sun is, as previously mentioned, essentially zero. Therefore intermediate possible alignments (paths that lead to the Sun) must be deterministically evaluated along the photon's zigzagged random walk trajectory. At each emission, scattering, or refraction and reflection boundary crossing event, the probability of a direct deterministic contribution to the detectable signal is computed. Computation of such a contribution depends on the feasibility to propagate the photon directly to the Sun through refraction and/or reflection from system interfaces.

The probabilities associated with the direct deterministic contributions are progressively scored in a tallied final weight, which cumulatively provides both the statistically reconstructed mean radiometric signal and the variance of the mean.[10] To avoid unnecessarily low contributions and high computational times, an *ad hoc* choice is made to limit deterministic contribution paths to one intermediate reflection or refraction at most. We refer to such deterministic contributions as virtual photons to distinguish them from real randomly tracked photons that are the object of the MC stochastic game. If a virtual photon encounters a totally absorbing boundary while propagating in the direction of incoming solar flux, its contribution to the detected signal is null.

The effects of wind-blown capillary waves that roughen an otherwise flat sea surface can be accounted for. Depending on the nadir angle of the incident photon and of the sea surface tilted wavelet normal, and on their relative azimuthal differences, the directions of reflected and transmitted photons (both real and virtual) are determined by use of geometrical-optics computations,[14] and their weight is adjusted according to effective surface interactions.[18] Wave facet occultation by nearby waves is not accounted for.

Virtual photons that propagate from the detector point (i.e., from the first event) are called first deterministic contributions (FDCs), and all other propagated virtual photons (from significant boundary crossing or from collision points) are subsequent deterministic contributions. FDCs to in-water downwelled quantities are directly obtainable after one sea–air transmission. On the other hand, FDCs to in-water upwelled quantities are obtainable for the given atmosphere–ocean system only through a sea floor Lambertian reflection followed by a sea–air boundary transmission according to Snell's law of refraction.

Lambertian reflection is a stochastic process with a defined ADF, and it represents an event not dissimilar, from a computational point of view, to a scattering process. Here we do not retain directional stochastic redistribution processes and thus scattering and Lambertian reflection events as intermediary events within FDCs. Therefore in-water upwelled quantities never score a FDC. In contrast, above-water upwelled quantities that result from the directional nonstochastic process of specular reflection from a flat ocean surface do allow for FDCs. Subsequent deterministic computations could occur for both above-water, in-water, downwelled, and upwelled quantities alike.

First and subsequent deterministic contributions to both downwelled and upwelled quantities fail to score if their path toward the Sun is blocked by a totally absorbing object (e.g., the tower structure).

3. Code Validation

The forward version of the PHO-TRAN MC code, including all the physics addressed in the current backward version, has been described and benchmarked on plane-parallel systems elsewhere.[11] Its backward MC version has been validated by Doyle[12] versus other radiative transfer codes and systems taken

from Mobley *et al.*[18] and with an additional finite-element code developed by Bulgarelli *et al.*[19] The completely 3-D radiative transfer MC computation scheme has also been recently validated with real *in situ* data, as shown by Zibordi *et al.*,[7] thus demonstrating its ability to handle field data effectively and to reproduce shadowing perturbations that affect the optical measurements collected at a specific oceanographic tower site as a function of wavelength, deployment distance from tower, above-water and in-water IOPs, and illumination conditions. A further validation of the 3-D backward MC simulation techniques is presented here for a selection of cases taken from the literature. Reference is made to the research of Gordon[1] on ship shading and of Gordon and Ding[9] on instrument self-shading.

A. Validation of Ship-Shading Computations

Perturbations on optical measurements induced by ship-shading have been analyzed by Gordon,[1] assuming a flat, totally absorbing 38.4 m by 6.55 m ship floating on homogeneous and infinitely deep oceanic waters, with $n_{oce} = 1.34$ (or, in some simplified cases, with unitary n_{oce}). Downwelling and upwelling irradiance profiles, as well as upwelling radiance profiles within an infinitesimally small nadir FOV, have been simulated as if measured by a pointlike detector along a horizontal reference line (azimuth angle of 0°) centered on and perpendicular to the longer side of the ship, under both totally clear (i.e., the sky is black) and overcast conditions. The latter illumination condition is what originates from a sky that provides a totally isotropic above-water incident radiance (as produced by a cosine-law incident photon flux). The index of refraction of the sky that contains either a void or an overcast atmosphere is assumed unitary: $n_{atm} = 1.00$. The P_{tot} used for the aquatic medium is tabulated in Gordon *et al.*[20] under the label *KA*. The θ_0 angle is positive from the vertically upward direction, while ϕ_0 is assumed to increase counterclockwise from the reference line. In-water total IOPs ($c \equiv c_{tot}$, $\omega_0 \equiv \omega_{tot}$), solar position ($\theta_0$, ϕ_0, including the overcast sky situation), measurement depth (d) from the sea surface, and distance (X) from the ship's center point are variable parameters. For brevity in subsequent notation, we omit the tot index when not introducing ambiguities (and the total single-scattering albedo will be simply indicated by ω_0, in agreement with much of what appears in the literature). A forced-collision sampling technique (see Appendix A) is employed within the water to prevent photons from leaving the aquatic medium or to interact with its sea–void interface, and the ship is treated as if suspended just above the interface (i.e., simulation method III in Gordon[1]).

Simulated shadowing percentage relative errors ϵ are defined as

$$\epsilon = \epsilon_{\Re} = \Delta\Re/\Re \times 100, \tag{1}$$

where $\Delta\Re = \Re - \tilde{\Re}$, and $\Re$ is the unperturbed and $\tilde{\Re}$ is the shadow-perturbed radiometric quantity ($\Re \equiv E_d$ or E_u or L_u and $\tilde{\Re} \equiv \tilde{E}_d$ or $\tilde{E}_u$ or $\tilde{L}_u$). The ϵ values have been computed with the PHO-TRAN MC code for all the cases considered by Gordon,[1] but for brevity only some of them are presented here. The qualitative comparison of data in Fig. 1 with the equivalent figure given in Gordon[1] exhibits close agreement. Error bars centered on the points indicate the ± 1 standard deviation σ, which provides the estimated statistical uncertainty on the PHO-TRAN MC computations of the percentage relative errors plotted in the figures, according to

$$\sigma = \sigma(\epsilon) = \mathrm{var}^{1/2}(\Delta\Re)/\Re \times 100. \tag{2}$$

The denominator $\Re$ in Eq. (2) is assumed to be a statistically constant value, because it is used in Eq. (1) only to normalize $\Delta\Re$ and thus can be simply removed from the square-root-of-the-variance, $\mathrm{var}^{1/2}$, operation together with the 100 factor. Quantitative values of upwelled nadir radiances, irradiances, and of shadowing-error-related quantities are presented in Table 1 and are compared with tabulated reference data (see Table III in Gordon[1]). Estimated mean upwelling nadir radiance L_u (W m^{-2} sr^{-1}) is given together with its standard deviation σ and statistical relative error (SRE) at the 1σ level. The mean difference between the unshaded L_u and shaded $\tilde{L}_u$ values, with corresponding σ and SRE at the 1σ level, and percentage relative error between shaded and unshaded L_u signals are also given (the latter is also given for E_u). Computations have been carried out just beneath the top of a homogeneous

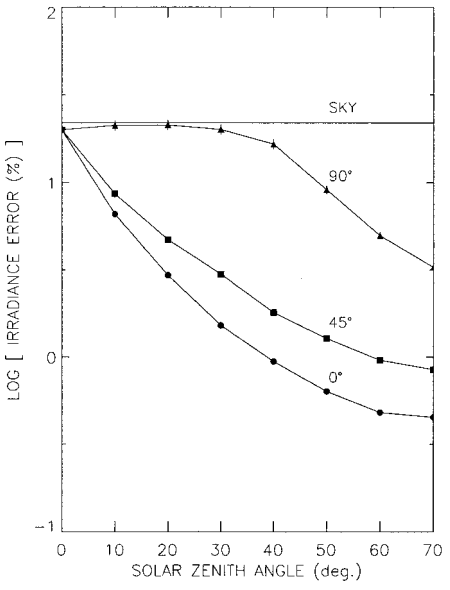

Fig. 1. Ship-shadowed E_d relative errors (log of percentage), estimated with the PHO-TRAN MC code as a function of θ_0, for three ϕ_0 angles ($\phi_0 = 0°$, circles; 45°, squares; 90°, triangles) and uniform incident radiance distribution (sky). Other parameters are $d = 30$ m, $X = 4.5$ m, $\omega_0 = 0.9$, and $c = 0.1$ m^{-1}. To be compared with Fig. 3 in Gordon's work.[1] Vertical error bars centered on the points indicate the $\pm 1\sigma$ estimated statistical uncertainty of the PHO-TRAN MC computations (error bars might not be visible if contained within the plotted symbol).

Table 1. Comparison of the Gordon and the PHO-TRAN MC Estimates[a]

Radiometric Quantity (at 0^-)	$g = 0$		$g = 0.750$		$g = 0.875$		$g = 0.950$		*KA*		*KA′*	
	Gordon	PHO-TRAN	Gordon	PHO-TRAN	Gordon	PHO-TRAN	Gordon	PHO-TRAN	Gordon	PHO-TRAN	Gordon	PHO-TRAN
L_u	0.08122	0.08119	0.02019	0.02021	0.00825	0.00855	0.00256	0.00251	0.01113	0.01069	0.01045	0.01022
L_u:σ	0.00132	0.00014	0.00100	0.00015	0.00115	0.00018	0.00197	0.00022	0.00348	0.00060	0.00061	0.00014
L_u:SRE	0.01630	0.00180	0.04950	0.00710	0.13940	0.02160	0.76950	0.08840	0.31260	0.05570	0.05830	0.01360
$(L_u - \tilde{L}_u)$	0.01016	0.01013	0.00249	0.00257	0.00096	0.00103	0.00029	0.00030	0.00157	0.00102	0.00102	0.00098
$(L_u - \tilde{L}_u)$:σ	0.00049	0.00006	0.00044	0.00006	0.00059	0.00007	0.00068	0.00008	0.00187	0.00010	0.00026	0.00006
$(L_u - \tilde{L}_u)$:SRE	0.04820	0.00600	0.17670	0.00240	0.61450	0.07120	2.34480	0.26670	1.19100	0.09800	0.25490	0.02330
$(L_u - \tilde{L}_u)/L_u$ in %	12.50	12.48	12.30	12.72	11.60	12.10	11.30	12.03	14.10	9.53	9.70	9.59
$(E_u - \tilde{E}_u)/E_u$ in %	21.30	21.27	14.50	13.74	12.20	12.55	14.20	14.94	14.70	14.90	14.20	14.14

[a]The estimates are of absolute values (means, standard deviations σ, and SRE) of unperturbed and ship-shadow perturbed radiometric quantities. Results are given as a function of the in-water Henyey–Greenstein phase function (variable asymmetry parameters g) and for two separate phase functions (*KA* and *KA′*).

and semi-infinite aquatic medium of unitary refractive index, with $c = 0.1\ \mathrm{m}^{-1}$, $\omega_0 = 0.8$, $\theta_0 = 0°$, $E_0 = 1.0\ \mathrm{W\,m}^{-2}$, and $X = 4.5$ m (following Gordon[1]). On top of the water lies a semi-infinite void region of unit refractive index. Results are given for various single-term Henyey–Greenstein (STHG) scattering phase functions, with asymmetry parameter $g = 0$ (isotropic scattering), 0.750, 0.875, 0.950 (highly peaked function), and for the strongly forward-peaked *KA* phase function[20] and its δ-truncated counterpart *KA′*.[1] We performed MC simulations for both codes by tracking 10^5 photons.

B. Validation of Instrument Self-Shading Computations

Similar to ship-shading, Gordon and Ding[9] analyzed instrument self-shading perturbations, assuming that a flat and totally absorbing circular instrument (i.e., a disk) floats on homogeneous and infinitely deep ocean waters with $n_{oce} = 1.338$ under both clear and overcast skies.

The general MC simulation framework, assumptions, procedures, and system parameters are similar to those defined in the previous ship-shading study (in particular they refer to simulation method III in Gordon[1]) and are modified by assuming only that the flat rectangular ship is replaced by a flat circular instrument casing of radius R, to which a sensor is centrally positioned on the lower face of the disk at depth $d = 0^-$ m (i.e., just beneath the sea surface). However, it must be noted that the symmetry of the sensor–instrument subsystem with respect to rotations in the horizontal plane reduces the overall radiative transfer problem to an azimuthally independent one. In our study system parameters and properties reflect exactly those defined in the study by Gordon and Ding. In-water total IOPs (c or a and ω_0) and solar position (θ_0 and overcast) are variable parameters. A cylinder of height $h = 1.0 \times 10^{-3}$ m and instrument radius $R = 1$ m has been used within the PHO-TRAN code to simulate the geometry of the shadow-casting instrument introduced in this otherwise plane-parallel atmosphere–ocean system.

In agreement with Gordon and Ding[9] shadowing percentage relative errors ε, defined by Eq. (1), are provided as a function of the product of radius R multiplied by c (or by a), for different in-water ω_0 values, and at a fixed θ_0, or under overcast skies (the previous IOPs represent total in-water coefficients). The PHO-TRAN MC estimated ε values for the simulated atmosphere–ocean–instrument system have been computed for all cases considered by Gordon and Ding,[9] some of which are presented in Fig. 2. Error bars centered on the points represent the ±3σ standard deviations on the estimated ε. The qualitative agreement between the two independent simulations is extremely high in all cases.

C. Forced-Collision Sampling Technique

We performed the above 3-D validation simulations following the methodologies described in Refs. 1 and 9, i.e., by suspending the shadow-casting object (ship

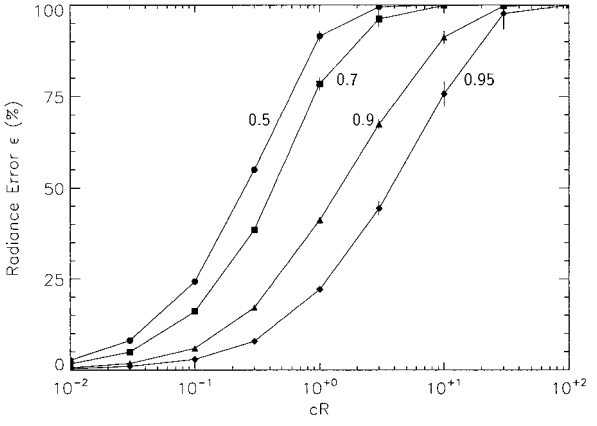

Fig. 2. Instrument self-shadowed L_u relative errors (percentage), estimated with the PHO-TRAN MC code as a function of cR for different ω_0 values ($\omega_0 = 0.5$, circles; 0.7, squares; 0.9, triangles; 0.95, diamonds). Solar zenith is $\theta_0 = 30°$. This figure is to be compared with Fig. 2 in the Gordon and Ding paper.[9] Vertical error bars centered on the points indicate the ±3σ estimated statistical uncertainty of the PHO-TRAN MC computations (error bars might not be visible if contained within the plotted symbol).

Table 2. Comparison of the Gordon and the PHO-TRAN Backward MC Simulations[a]

MC Simulation	ϕ_0 =	ϵ_{E_d} (5 m) 0°	45°	90°	ϵ_{E_d} (40 m) 0°	45°	90°
I Gordon		1.27	1.43	2.36	3.98	5.80	15.88
I PHO-TRAN		1.33	1.52	2.47	3.83	5.76	15.69
III Gordon		0.43	0.60	1.57	4.01	5.71	15.71
III PHO-TRAN		0.40	0.58	1.55	4.05	5.62	16.04

[a]Included are percentage relative error values for ship-shadowed E_d at 5- and 40-m depth and variable solar azimuth. Two simulation techniques were adopted: I, ship's hull in the water; III ship's hull above the water and no surface interactions allowed.

Table 3. Comparison of the Gordon and the PHO-TRAN Backward MC Simulations[a]

MC Simulation	ϕ_0 =	ϵ_{E_u} (0^- m) 0°	45°	90°	ϵ_{L_u} (0^- m) 0°	45°	90°
I Gordon		7.74	8.13	8.95	3.33	4.30	8.96
I PHO-TRAN		8.40	8.78	9.92	3.61	4.57	9.97
III Gordon		7.81	8.22	9.01	3.17	3.98	8.83
III PHO-TRAN		7.90	8.17	9.16	3.22	3.95	8.90

[a]Included are percentage relative error values for ship-shadowed E_u and L_u at 0^--m depth and at variable solar azimuths. The same simulation techniques as in Table 2 were adopted.

or instrument) just above the sea–void interface and by forcing collisions on upward-moving photons before they reached that interface, thereby precluding photons to interact with it and with the suspended shadowing structure. In this case computations account for direct shadowing only, and neglect second or higher-order shadowing effects.

This simulation technique is not, however, the only one, as already pointed out by Gordon,[1] although it is quite fast and under most conditions leads to results similar to those of other simulation approaches. Nonetheless, some characteristic effects of this particular technique are observed especially at shallow optical depths just beneath the water surface: the photon in this approximation never interacts directly with the interface (or the ship or the instrument), and the shadowing error is underestimated because interaction with the surface (and the ship or the instrument) does in fact occur.

Simply considering the ship case different simulation techniques have been examined by Gordon in addition to method III.[1] His simulation I refers to ship hull in the water and photons that do not interact with the surface; simulation II refers to ship above water and photons that interact with the surface. To further and quantitatively illustrate and validate the effects of the different simulation approaches, part of the data in Tables IV and V from Gordon's work are reproduced and compared with PHO-TRAN MC simulations in Tables 2 and 3, respectively (for methods I and III only). Computations have been carried out within a homogeneous and semi-infinite aquatic medium of refractive index $n_{oce} = 1.34$ with $c = 0.1\ m^{-1}$, $\omega_0 = 0.9$, $\theta_0 = 20°$, and $X = 4.5$ m. On top of the water lies a semi-infinite void region of unit refractive index. Results are computed at three solar azimuths: $\phi_0 = 0°, 45°, 90°$. We carried out MC simulations for both codes by tracking 10^5 photons.

We then consider a further simulation scheme by submerging the ship just beneath the sea–void interface and by allowing photon interactions with the surface. In this case, a photon undergoing random walk and in the presence of a submerged and totally absorbing ship hull can completely stop contributing to the detected signal, because it could be killed when it hits the hull. No further deterministic contributions to the detected signal can be obtained from this photon history, and both second- and higher-order shadowing effects are taken into account. The twin correlated photon, i.e., tracked in the absence of the ship, which can now interact with the sea–void interface also at points that belong to the ship-removed area, can now be totally internally reflected or forced to do so by adjustment of the photon's weight through an appropriate Fresnel reflectivity coefficient. This inner reflected photon can continue to contribute positively to the detected signal by further deterministic contributions, thus increasing the unshaded signal. This raises the relative difference between shaded and unshaded signals, thus increasing the shadowing effect.

As an example of how the shadowing-error can vary, results for ship and surface interacting photons are overplotted to results generated for noninteracting photons in an otherwise identical system. The downwelling irradiance shadowing error that we computed by ignoring interactions with the sea surface or the ship's hull is shown in Fig. 3 as filled symbols and continuous curves. Open symbols and dashed curves are used to represent interactions with the sea surface and the ship's hull. It is noteworthy to observe that just beneath the surface, when we allow for interface interaction, all the plotted shadowing errors converge, and that within the first few meters depth the diffuse (sky) shadowing error increases much more rapidly than the other shadowing errors. Moreover, the shadowing errors in two cases (ϕ_0 at 0° and 45°) are larger than the errors that correspond to the not-surface-interacting cases, although they remain small in absolute value. In fact, it must be noted that the variations seen at low shadowing values in Fig. 3, with the error axis on a base 10 logarithmic scale, are small variations on a linear scale (i.e., logarithmic shadowing errors lower than 0% correspond to linear shadowing errors of between 0% and 1%).

If a scattering atmosphere is allowed for, the previous considerations are even more relevant. In fact, photons allowed to escape by transmission through the sea–air interface within the ship-removed area (and not only those totally reflected) can continue to contribute positively to the detected signal, since other scattering events and related deterministic contributions can occur in the atmo-

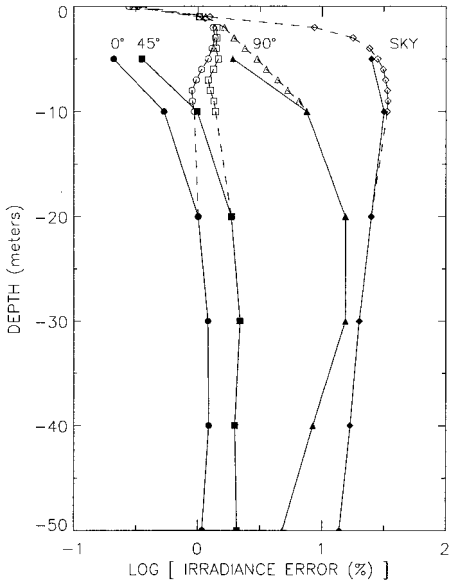

Fig. 3. Ship-shadowed E_d relative errors (log of percentage), estimated with the PHO-TRAN MC code as a function of in-water sensor depth d, for three solar azimuth angles ϕ_0 ($\phi_0 = 0°$, circles; 45°, squares; 90°, triangles) and a uniform incident radiance distribution (sky, diamonds). Values for the other parameters used in these simulations are $X = 4.5$ m, $\theta_0 = 40°$, $\omega_0 = 0.9$, and $c = 0.1$ m^{-1}. The filled symbols and continuous curves identify the results that were obtained when photon interactions with the sea surface and with the ship's hull were completely ignored, whereas additional simulations that allow for photons to interact with the sea surface and with the submerged ship's hull are overplotted with open symbols and dashed curves, at 1-m-deep increments within the 10-m top ocean layer. Horizontal error bars that indicate the $\pm 1\sigma$ estimated statistical uncertainty of the PHO-TRAN MC computations are not visible because they are completely enclosed within the plotted symbol.

sphere. Moreover, when in the presence of a scattering atmosphere, this simulation technique allows for photons that have made their way through the sea–air interface to collide with the ship also from above (after atmospheric scattering) and to be removed from the MC simulation, thus contributing negatively to the detected signal. This technique will be retained in further simulations that pertain to tower-shading evaluations, because complete allowance for photon interaction with the intervening media interfaces and absorbing structures is required, especially when we evaluate the shadowing error at shallow optical depths, close to the shadow-casting object, and in the presence of a scattering atmosphere.

To allow for interactions of photons with the sea–air interface and with objects above it, the forced-collision sampling scheme is adopted within PHO-TRAN MC simulations for both submerged and emerged photons. The scheme is applied to photons transported to the TOA or the lateral boundaries of the system, and these are taken to be the only surfaces within which a forced collision must take place.

4. Shadowing Sensitivity to System Parameters

With the aim of evaluating and removing the shadowing perturbation effects that occur on *in situ* submerged radiance and irradiance measurements acquired in the proximity of large and complex 3-D deployment structures, we have defined a realistic reference atmosphere–ocean system model. This model has provided the framework within which PHO-TRAN MC simulations have been conducted to generate extensive 3-D radiative transfer computations and thereby to estimate shadowing percentage relative errors. Whereas some assumptions of the underlying system must be made, care has been given to describe the modeled system in a highly realistic and accountable way.

Computations have been initiated by systematically varying all the relevant geometric, environmental, and optical parameter values that describe our reference model for the Sun–atmosphere–ocean–structure–detector system. Correction factors have been generated to account for the shadowing perturbation caused by the AAOT located in the northern Adriatic Sea. The sensitivity study has thus ensured the determination of the system parameters and parameter values and ranges, most significantly contributing to tower-shading perturbation of the in-water light field that surrounds the measurement point.

A. Reference Atmosphere–Ocean System Modeling

The reference model that describes the atmosphere–ocean system propagation media, geometry, boundary conditions, and IOPs as a function of monochromatic radiation of a given wavelength λ that belongs to the visible and the near-infrared spectrum is designed by use of system parameters and parameter values discretely distributed over adequate ranges for the relevant data: (i) measured or derived at the investigated site (including data obtained from climatological models or from Earth-observation satellite data), (ii) originated from accepted atmospheric models, and (iii) from accepted oceanic models.

1. Site Characteristics, Measurements, and Oceanographic Tower Modeling

The AAOT measurement site is located in the northern Adriatic Sea (45.31 °N, 12.51 °E) approximately 8 nautical miles southeast of the Venice Lagoon. The average water depth immediately below the tower is 17 m, and the composition of the sea floor is primarily sand and silt. According to Berthon *et al.*[21] the study area is characterized mostly by moderate case 2 water determined by the fresh waters from the northern rivers and by coastal aerosol determined by the continental aerosols from the nearby Po Valley. Nevertheless, the site can also exhibit purely maritime aerosol and case 1 seawater features. Owing to these characteristics the site is representative of the environmental variability found in the northern Adriatic Sea region.

Ocean color radiometers OCR-200 and OCI-200 from Satlantic (Halifax, Nova Scotia) positioned on the wire-stabilized profiling environmental radiometer (WiSPER) are routinely used at the AAOT bio-optical calibration and validation oceanographic site to measure the in-water light field in the visible and the near-infrared spectral regions at nominal center wavelengths of $\lambda = 412$, 443, 490, 510, 555, 665, and 683 nm. We recorded the in-water light field by vertically profiling the water column at a 6-Hz sampling rate, i.e., ensuring data at less than 2-cm intervals at the nominal WiSPER profiling speed ($\approx$0.1 m s^{-1}). Measurements of shadow-perturbed downwelling spectral irradiance $\tilde{E}_d(z, \lambda)$, upwelling spectral irradiance $\tilde{E}_u(x, \lambda)$, and upwelling spectral radiance $\tilde{L}_u(z, \lambda)$, where z is the geometric depth below the water surface, are taken at a fixed deployment distance of 7.5 m from the AAOT legs, toward the southeast. The $\tilde{E}_d(z, \lambda)$, $\tilde{E}_u(z, \lambda)$, and $\tilde{L}_u(z, \lambda)$ underwater profiles, corrected for instrument self-shading effects,[22] are used as objective data to which tower-shading removal is applied, assuming self-shading independent of tower-shading perturbations.

A relevant number of system parameter values was derived from the observed ranges of variability of the following quantities (directly measured or retrieved at the AAOT site for the period October 1995–December 1998): angles θ_0 and ϕ_0, directly required by the modeled system; aerosol Ångström exponent α and coefficient ν were used to obtain the range of variability for the atmospheric column aerosol optical depth τ_{aer} [as derived from measurements of direct solar irradiance $E_s(0^+, \lambda)$, taken with a sunphotometer from CIMEL Electronique, Paris, France, CE-318 at nominal wavelengths of $\lambda = 340$, 380, 440, 501, 675, 870, and 1020 nm]; above-water downwelling total $E_d(0^+, \lambda)$ and diffuse $E_i(0^+, \lambda)$ irradiances [taken with a Yankee Environmental Systems (Turners Falls, Mass.) MFR-6 rotating shadow-band radiometer at nominal wavelengths of $\lambda = 415$, 500, 610, 665, 862, and 960 nm], used to obtain the range of variability for the diffuse over direct above-water irradiance ratio $I_r(0^+, \lambda) = E_i(0^+, \lambda)/E_s(0^+, \lambda)$; profiles of hydrosol (total minus pure seawater) beam attenuation, $c_{hyd}(z, \lambda)$, and absorption, $a_{hyd}(z, \lambda)$, coefficients [taken with a WET Labs (Philomath, Oreg.) AC-9 absorption–attenuation meter at nominal wavelengths of $\lambda = 412$, 440, 488, 510, 555, 630, 650, 676, and 715 nm] used to define the range of variability of seawater IOPs (and to compute $b_{hyd} = c_{hyd} - a_{hyd}$ and $\omega_{hyd} = b_{hyd}/c_{hyd}$); atmospheric pressure A_p used to obtain the range of variability for the atmospheric column molecular optical depth τ_{mol}; ozone absolute load (as derived, for example, with the Total Ozone Mapping Spectrometer data) used to compute the variability in the atmospheric column ozone optical depth τ_{ozo}.

The AAOT structure is modeled as completely absorbing. Simulated pointlike detectors that measure downwelling and upwelling irradiance and upwelling radiance are positioned at variable locations with respect to the tower. Figure 4 shows the AAOT schematic 3-D geometry and linear dimensions as modeled within the PHO-TRAN MC code. The above tower structure is modeled with a few simple and joined rectangular blocks, included in a maximum volume of no more than approximately 12.5-m height by 8.5-m width by 9.8-m depth, to which the optics-deployment platform is joined at 6.5-m height and pointing exactly toward the southeast. Tower pillars with horizontal dimensions of 0.8 m by 0.8 m are vertically submerged to 17.0 m in the water with 3.8 m above water.

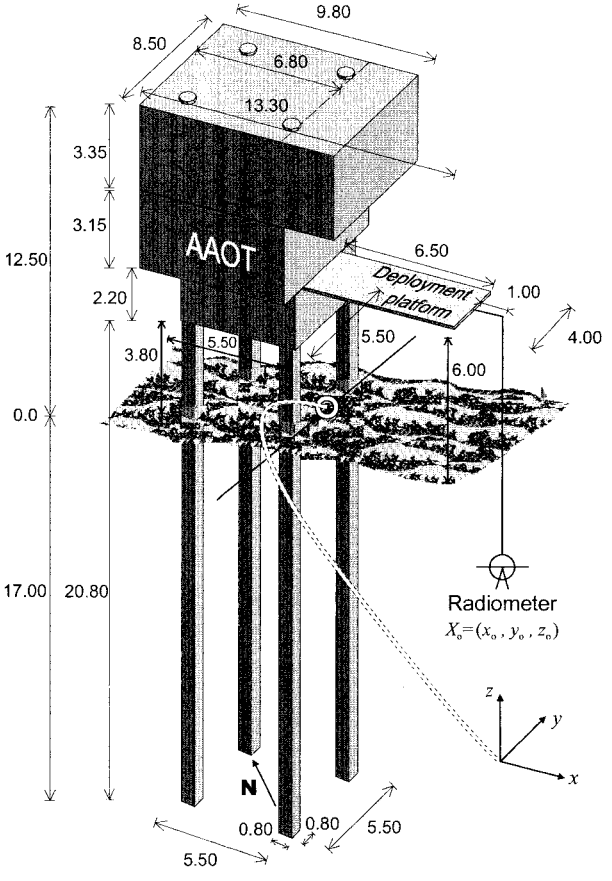

Fig. 4. AAOT schematic 3-D geometry as modeled within the PHO-TRAN MC code; distances are shown in meters and surfaces are assumed black. The south–north direction intersects two opposite angular AAOT pillars as shown by the N arrow that points to the north. Optical radiometers are deployed at 7.5 m from the tower legs (along the vertical line through the indicated Radiometer). The orthogonal x-y-z axes origin is placed on the sea surface and between the southern and southeastern tower legs. Radiometers are placed at $X_0 = (x_0, y_0, z_0)$.

2. *Atmospheric Modeling*

The Sun is a point light source at infinity whose extra-atmospheric irradiance value, $E_0(\lambda)$, is taken from Neckel and Labs[23] at the nominal central wavelength of the radiometer. The mean Earth–Sun distance is assumed (in fact shadowing-error computations do not require a day-of-the-year dependent approach). The atmosphere is divided into 14 plane-parallel layers for the aerosol, gas molecules,

and ozone vertical distribution. The TOA is positioned 60 km above the sea surface, and the boundaries among the 14 atmospheric layers are set at 0.5, 1.0, 2.0, 3.0, 6.0, 10.0, 15.0, 20.0, 25.0, 30.0, 35.0, 40.0, and 50.0 km above the sea surface. We chose this layering to optimize the stepping—also by use of a relatively small number of layers—of the three concurrent OSC profiles typically found in the atmosphere. Each atmospheric layer contains a variable mixture of ozone (only absorbing), other gas molecules (only scattering), and aerosol (here assumed only scattering). The spectral vertical profile of the ozone relative concentration is computed in agreement with Lacis and Hansen[24] and Vigroux.[25] The spectral vertical profile of the molecular (i.e., Rayleigh scattering gases) optical depth is computed according to Margraaf and Griggs,[26] Frölich and Shaw,[27] and Young.[28] The spectral vertical profile of the aerosol optical depth is modeled according to Ångström[29] and Elterman,[30] assuming an aerosol scale height of $H = 1.2$ km. The molecular scattering at angle ψ is described by the Rayleigh phase function $P_{\mathrm{mol}}(\psi) = 3/16\pi \times (1 + \cos^2\psi)$. The aerosol scattering at angle ψ is approximated by the spectral two-term Henyey–Greenstein (TTHG) analytical function $P_{\mathrm{aer}}(\psi; \lambda) = \gamma P_{\mathrm{HG}-g_1}(\psi) + (1 - \gamma)P_{\mathrm{HG}-g_2}(\psi)$, where $P_{\mathrm{HG}-g}(\psi)$ is the STHG phase function,[31] $P_{\mathrm{HG}-g}(\psi) = 1/4\pi(1 - g^2)(1 + g^2 - 2g\cos\psi)^{-3/2}$, and the asymmetry parameters (g_1, g_2) and forward-to-backward peak ratio (γ) are spectrally dependent quantities, as given by Sturm and Zibordi.[32] The sea surface is assumed flat and foam free. This latter assumption is made because most of the *in situ* measurements taken at the AAOT site have been performed with wind speeds v of less than 5 ms^{-1}.

3. Oceanic Modeling

The seawater volume is divided into 15 plane-parallel layers that contain a variable mixture of pure seawater (absorbing and scattering) and suspended plus dissolved constituents (absorbing and scattering). The sea bottom is 17 m below the sea surface, and boundaries between the 15 oceanic layers are set at each meter depth starting at 1.5 m below the sea surface (the bottom layer is between the 14.0-m depth and the sea floor). The layer compositions are spectrally assigned according to typical in-water vertical profiles of the hydrosol $c_{\mathrm{hyd}}(z, \lambda)$ and $a_{\mathrm{hyd}}(z, \lambda)$ coefficients associated with suspended plus dissolved constituents. The pure seawater spectral absorption coefficient $a_{\mathrm{wat}}(\lambda)$ is from Pope and Fry,[33] the pure seawater spectral scattering coefficient $b_{\mathrm{wat}}(\lambda)$ is from Buiteveldt[34] (giving $c_{\mathrm{wat}} = a_{\mathrm{wat}} + b_{\mathrm{wat}}$). Pure seawater scattering at angle ψ is modeled according to the Einstein–Smolouchowski theory,[17] with a Rayleigh-like scattering phase function $P_{\mathrm{wat}}(\psi) = 3/4\pi \times (3 + q)^{-1}(1 + q\cos^2\psi)$, where q is the polarization factor, which is equal to 0.84 according to Morel.[35] We use the typical hydrosol phase function $P_{\mathrm{hyd}}(\psi)$ as extrapolated by Mobley *et al.*[18] from the measurements taken by Petzold[36] in the San Diego harbor. The sea floor is assumed Lambertian, with known r_b as obtained from averaging experimental measurements of the irradiance reflectance ratio taken by Zibordi *et al.*[37] at the site's sea floor (its reflectance, a ratio of irradiances, is supposed to be independent of tower-shading effects since the irradiance perturbations on downward and upward components are assumed small and comparable).

B. Tower-Shading Effects

Tower-shading effects are established based on correlated sampling estimations of the AAOT perturbed ($\tilde{\Re} \equiv \tilde{E}_d$ or $\tilde{E}_u$ or $\tilde{L}_u$) and unperturbed ($\Re \equiv E_d$ or E_u or L_u) radiometric quantities, evaluated by performing complete 3-D backward MC simulations within specific Sun–atmosphere–ocean–AAOT–detector systems based on the previously described reference system.

Within this system, the origin of the right-handed orthogonal axes set is placed at a point centered on the line that connects the southern and the southeastern tower legs and lying on the horizontal atmosphere–ocean interface (as illustrated in Fig. 4). Positive coordinates for the horizontal x axis and the vertical z axis increase toward the southeast and upward directions, respectively. Simulations are performed at different wavelengths, at different depths, and at different distances, including the fixed distance of 7.5 m to the southeast of the southern tower leg, where the WiSPER optics instrumentation is normally lowered from a deployment platform. The direction $\Theta_0 = (\theta_0, \phi_0)$ to solar point is assigned with θ_0 measured from the local vertical and ϕ_0 measured counterclockwise from the positive x axis (i.e., the deployment platform axis) and is therefore linked to ϕ_0', the ordinary azimuth compass reading, by $\phi_0 = 135° - \phi_0'$. This ϕ_0 definition allows symmetrical considerations to be made for the AAOT deployment platform axis and is retained within the PHO-TRAN coordinate reference system adopted for AAOT shadowing investigations. Photons are released from the radiometer located at a point $X_0 = x_0, y_0, z_0$ according to its ADF and are backtracked to the Sun, following the backtracking algorithms previously outlined, and by use of the variance reduction techniques described in Appendix A.

Tower-induced shadowing percentage relative errors $\epsilon_{\Re}$ (ϵ_{E_d}, ϵ_{E_u}, ϵ_{L_u} in separate notation) between $\tilde{\Re}$, the *in situ* AAOT shadow-perturbed radiometric quantity, and $\Re$, the related far-field unperturbed radiometric quantity, are defined by Eq. (1). Tower-shading effects are then completely defined by $\epsilon_{\Re}$ and by the set of system parameter values used to describe the corresponding Sun–atmosphere–ocean–AAOT–detector system.

C. Sensitivity Study

A tower-shading sensitivity study has been undertaken to determine the system parameters that predominantly influence AAOT shadowing of the in-

Table 4. Standard Sun–Atmosphere–Ocean–AAOT–Detector Reference System[a]

Parameter	Unit	Data (λ = 412 nm)	Comments and Data Source
Latitude	deg (°)	45.3139 N	AAOT location
Longitude	deg (°)	12.5083 E	AAOT location
Date	dd/mm/yyyy	17/06/1999	Identifies specific campaign data
UTC	hh:mm	12:22	Identifies specific measurements
Solar zenith θ_0	deg (°)	22.70	Derived from the above data
Solar azimuth ϕ_0	deg (°)	−27.84	Derived in PHO-TRAN coordinates
Detector position X_0	(m,m,m)	[7.5, 0, 0^-]	0^- is taken as 10^{-4} m
Wavelength λ	nm	412	Radiometer specifications
TOA irradiance E_0 (λ)	W m^{-2} nm^{-1}	1.808	Neckel and Labs[23]
n_{atm}	—	1.00	Assumed
$\tau_{ozo}(\lambda)$ (total)	—	0.000663	327 Dobson units (TOMS data)
$\tau_{mol}(\lambda)$ (total)	—	0.318376	With A_p = 1013 hPa
$\tau_{aer}(\lambda)$ (total)	—	0.247725	CE-318 data (α = 0.053, ν = 1.74)
ω_{aer}	—	1	Aerosol single-scattering albedo
P_{mol}	sr^{-1}	$\frac{3(1+\cos^2\psi)}{16\pi}$	Rayleigh theory[38]
$P_{aer}(\lambda)$	sr^{-1}	TTHG	Sturm and Zibordi[32]
Sea surface	NA	flat	Assumed
n_{oce}	—	1.34	Assumed
$a_{wat}(\lambda)$	m^{-1}	0.00456	Pope and Fry[33]
$b_{wat}(\lambda)$	m^{-1}	0.00667	Buiteveldt *et al.*[34]
$a_{hyd}(\lambda)$ (top layer)	m^{-1}	0.11740	AC-9 data, Berthon *et al.*[21]
$b_{hyd}(\lambda)$ (top layer)	m^{-1}	0.42860	AC-9 data, Berthon *et al.*[21]
$\omega_{hyd}(\lambda)$ (top layer)	—	0.78	Derived from the above data
P_{wat}	sr^{-1}	$\frac{3(1+q\cos^2\psi)}{4\pi(3+q)}$	Einstein–Smolouchowski theory[39]
P_{hyd}	sr^{-1}	Petzold[36]	Mobley *et al.*[18] tabulation
Sea floor	NA	Lambertian	Assumed
Sea floor reflectance $r_b(\lambda)$	—	1.13	Zibordi *et al.*[37]

[a]The shadowing sensitivity analysis was performed with this system. TOMS, Total Ozone Mapping Spectrometer; NA, not applicable.

water light field that surrounds the measurement point. The AAOT percentage relative errors $\epsilon_{\Re}$ for E_d, E_u, and L_u at the normal optics-deployment location, and at a depth just beneath the sea surface, were first computed for a specific Sun–atmosphere–ocean–AAOT–detector system, hereafter called the standard system as defined in Table 4. This standard system assumes homogeneous atmosphere and ocean layers and is specifically constructed for solar radiation interactions that occur with matter at 412 nm. Departing from this standard system we conducted an extensive sensitivity analysis of $\epsilon_{\Re}$ to variations in all relevant system parameter values and present our results.

The sensitivity study results for $\epsilon_{\Re}$ are plotted in Figs. 5–14, including sensitivity to θ_0 (with fixed ϕ_0), to ϕ_0 (with fixed θ_0), to ϕ_0 (with coincident time-correlated θ_0, along high and low Sun-path orbits as occur during boreal summer and winter, respectively), to wavelength λ, to sensor depth z_0 (including considerations of water column stratification) and horizontal position (x_0 and y_0 separately), and to τ_{aer}, a_{hyd}, and b_{hyd} (with some considerations of sensitivity to P_{hyd}). Other results that do not show significant influence to the tower-shading effect have been omitted, which include sensitivity to τ_{ozo}, τ_{mol}, ω_{aer}, and P_{aer}. Further work could be carried out to assess extensive dependencies of $\epsilon_{\Re}$ on P_{hyd} and on sea surface wave-slope distribution. But since these parameters are difficult to evaluate, they have not been included in this study for the development of an operational correction scheme. A detailed analysis and discussion of the sensitivity study is provided in Section 5.

5. Sensitivity Analysis and Discussion

We present the analysis and discussion of the sensitivity study as a function of system parameters that most significantly influence the tower-shading effects, with reference to the data plotted in Figs. 5–14 and listed in Tables 5 and 6. These data are simulated at 0^--m depth, with the exception of the data in Fig. 9 where depth-dependent E_d, E_u, and L_u profiles are shown. In all the figures the curves are simply used to connect mean relative errors, and the symbols encompass the maximum statistical noise on PHO-TRAN MC simulations (at the 3σ confidence level).

A. $\epsilon_{\Re}$ versus θ_0

The $\epsilon_{\Re}$ results as a function of θ_0 are shown in Fig. 5 for fixed $\phi_0 = 0°$ (i.e., with the solar azimuth aligned along the AAOT deployment platform axis). The $\epsilon_{\Re}$ values exhibit a positive second derivative with respect to θ_0. This effect, which differs from the ge-

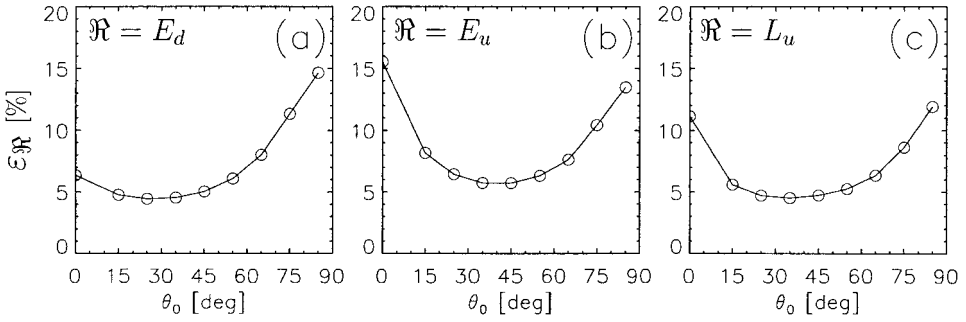

Fig. 5. AAOT tower-shading percentage relative errors (a) ϵ_{E_d}, (b) ϵ_{E_u}, (c) ϵ_{L_u} on subsurface E_d, E_u, and L_u for the standard case as a function of θ_0 with $\phi_0 = 0°$, i.e., the Sun projection on a horizontal plane moves along the AAOT deployment platform axis (ϕ_0 is measured on the PHO-TRAN AAOT coordinate reference system).

nerically monotonic decreasing behavior found for ship-shading effects under a black sky (e.g., Gordon[1]), is due to the increased total atmospheric optical path, $\tau_{atm}(\theta_0)$, traveled by the slanted solar rays. Under these conditions the atmospheric scattering, and thus the diffuse light regime, are increasing functions of θ_0. Consequently, the diffuse shadowing caused by the AAOT structure increases with θ_0 and prevails at the measurement point on the decreasing shadowing effects induced by the directly cast AAOT shadow (which are the only significant shadowing effects that perturb radiometric measurements in an atmosphere-removed case). In fact, at high solar zenith angles, the AAOT direct shadow moves away from the measurement point, and less significantly perturbs the light field at that point.

B. $\epsilon_\Re$ versus ϕ_0

The $\epsilon_\Re$ results as a function of ϕ_0 for two fixed θ_0 values are shown in Fig. 6, plotted for $\theta_0 = 30°$ and 75°. Only one (the negative) side of ϕ_0 is shown, because it is symmetrical with respect to the x axis (i.e., the $\phi_0 = 0°$ line). Note that the shadowing effect increases when ϕ_0 decreases. Starting from an initial illumination condition at $\phi_0 = 0°$ and keeping θ_0 constant, we found that the skylight at the measurement point is increasingly shadowed by the AAOT structure as $|\phi_0|$ increases. The shadowing increases at a different rate as $|\phi_0|$ moves through 90° and beyond. The two main factors responsible for the observed $\epsilon_\Re$ values are (i) the variable amount of total skylight shadowed by the tower and (ii) the variable shape, volume, and position of the AAOT direct in-water shadow. The latter factor affects the direct and indirect shadowing of the in-water sensor. For a given system, the overall magnitude of this effect and variability as a function of ϕ_0 depends on solar zenith. At low θ_0 the portion of skylight is low with respect to direct sunlight, whereas higher θ_0 values imply a relative increase in skylight. At low θ_0 the directly cast AAOT shadow is generally closer to the in-water sensor than for the high θ_0 cases, but is projected into smaller surface-water volumes. In the high θ_0 cases, a steeper increase in $\epsilon_\Re$ can be noted at $\phi_0 \approx -150°$. In fact, at the AAOT latitude for $|\phi_0| \approx 150°$ and $\theta_0 = 75°$, the deployment platform direct shadow is close to the WiSPER measurement point, thus increasing the total shadowing effect.

C. $\epsilon_\Re$ versus Θ_0

In Fig. 7 the $\epsilon_\Re$ results are plotted as a function of solar direction $\Theta_0 \equiv \theta_0, \phi_0$ with variable ϕ_0—and covarying θ_0—for a high (low) Sun trajectory. The solar track at the AAOT site is simulated by consideration of a series of solar positions at 0.5-h increments along a solar orbit traced in the sky during the

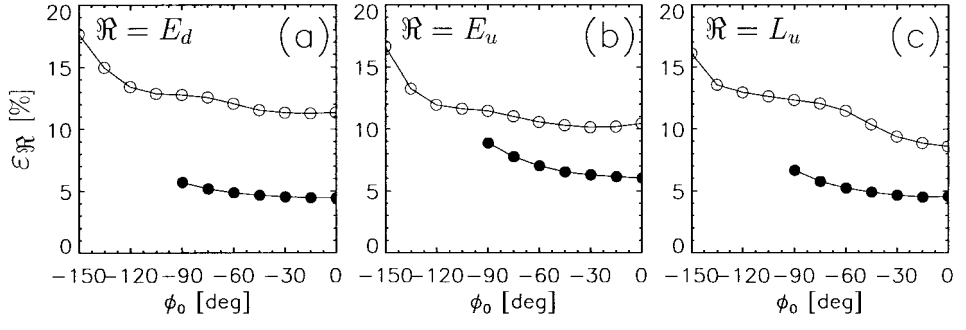

Fig. 6. AAOT tower-shading percentage relative errors (a) ϵ_{E_d}, (b) ϵ_{E_u}, (c) ϵ_{L_u} on subsurface E_d, E_u, and L_u for the standard case as a function of ϕ_0 with $\theta_0 = 75°$, i.e., a low Sun moves along an imaginary circular trajectory (open circles), and with $\theta_0 = 30°$, i.e., a high Sun moves along an imaginary circular trajectory (filled circles). Computations for $\theta_0 = 30°$ stop at $\phi_0 = -90°$ because the Sun never exceeds such a solar azimuth angle for the given $\theta_0 = 30°$ at the AAOT latitude.

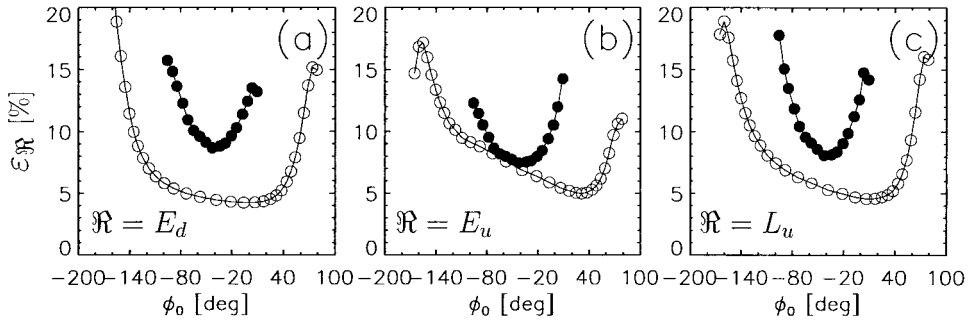

Fig. 7. AAOT tower-shading percentage relative errors (a) ϵ_{E_d}, (b) ϵ_{E_u}, (c) ϵ_{L_u} on subsurface E_d, E_u, and L_u for the standard case as a function of variable ϕ_0 (and covarying θ_0) along two real solar path orbits, and resolved at 0.5-h increments. The $\epsilon_\Re$ for a boreal summer (high Sun) orbit are shown as open circles; the filled circles represent a boreal winter (low Sun) orbit.

boreal summer (winter) solstice. This track represents a high and long (low and short) solar path, achieving a minimal solar zenith angle at approximately 22° (69°) from the vertical at 12:52 (12:48) UTC, or local noon, when the solar azimuth angle is at approximately −45° (or +180° on the compass). The abscissa axis is nonlinearly related to time of day t, and decreasing ϕ_0 corresponds to increasing t. Distinguishing features for the high solar path orbit are (1) a wide range of shadowing effects; (2) linearizable angular regions, in which the shadowing effect dependence on t can be approximated by straight lines; (3) comparable shadowing errors on E_d, E_u, and L_u; and (4) shadowing errors lower than 10% at the normal deployment time, i.e., close to local noon. Compared to the high solar path orbit the shadowing errors for the low solar path show (1) lower maximum values, but (2) higher minimum values; (3) less structured dependence on variable solar position, but (4) sharper features (i.e., the second derivative of $\epsilon_\Re$ with respect to ϕ_0 in the proximity of a minimum is higher than in the previous case); (5) comparable shadowing errors on E_d, E_u, and L_u; (6) shadowing errors close to 10% at the normal deployment time (on average, higher shadowing is found for these low solar path orbits, i.e., in winter).

The $\epsilon_\Re$ values as a function of variable ϕ_0—and of covarying θ_0—exhibit a sharp increase (with exponential growth trends) on the edges of the ϕ_0 variability range for the high solar path case shown in Fig. 7. This effect is due to the direct shadow cast by the AAOT deployment platform, shaped as a rectangular prism. When $\phi_0 < -120°$ and $\phi_0 > 40°$, the prism directly shadows the FOV of the radiometers, causing a remarkable and predictable increase in the shadowing effect. (This is usually avoided when one conducts *in situ* measurements). For the low solar path the same sharp increase is not present, whereas a strongly concave $\epsilon_\Re$ curve demonstrates the importance of skylight shadowing caused by the main AAOT structure. The shadowing effect smoothly increases as ϕ_0 departs from −45°, corresponding to the maximum solar elevation point (with $\theta_0 \approx 69°$) of this low Sun trajectory and to the conditions with the directly cast shadow on average being the closest to the measurement point. As ϕ_0 departs from −45° the diffuse component of the shadowing errors prevails on the direct component. The same behavior is found for the high solar path (for which the maximum solar elevation point corresponds to a minimal $\theta_0 \approx 22°$ and also identifies the minimum $\epsilon_\Re$ values).

D. $\epsilon_\Re$ versus λ

The $\epsilon_\Re$ results as a function of wavelength are shown in Fig. 8. Wavelength λ that characterizes all the related spectral quantities (E_0, τ_{ozo}, τ_{mol}, τ_{aer}, P_{aer}, r_b, and a_{wat} and b_{wat}, a_{hyd}, and b_{hyd}) varies from 412 to 665 nm through 443, 490, 510, and 555 nm. The shadowing error for E_d, influenced mainly by atmospheric IOPs, follows a spectral exponential decay

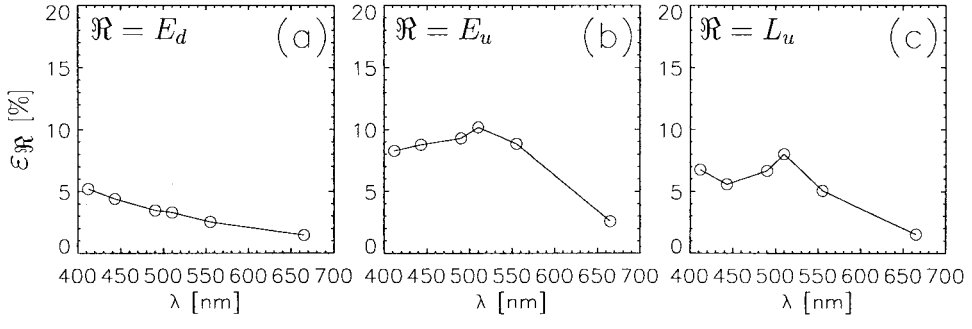

Fig. 8. AAOT tower-shading percentage relative errors (a) ϵ_{E_d}, (b) ϵ_{E_u}, (c) ϵ_{L_u} on subsurface E_d, E_u, and L_u for the standard case as a function of λ.

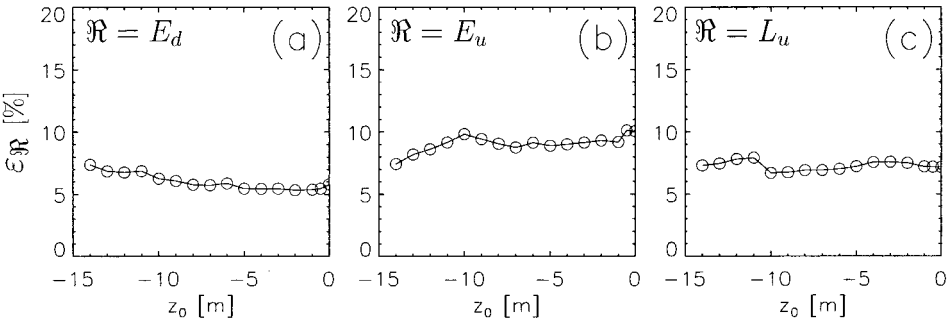

Fig. 9. AAOT tower-shading percentage relative errors (a) ϵ_{E_d}, (b) ϵ_{E_u} (c) ϵ_{L_u} on in-depth E_d, E_u, and L_u for the standard case as a function of sensor depth z_0 in a homogeneous water column.

that results from the increased direct light regime with wavelength, as caused by reduced atmospheric scattering. The shadowing errors for E_u and for L_u show more featured spectral dependence that is due to the more complex in-water scattering and absorption phenomena.

E. $\epsilon_{\Re}$ versus X_0

The $\epsilon_{\Re}$ results as a function of sensor position $X_0 \equiv x_0$, y_0, z_0 for independently variable depth z_0 and horizontal positions x_0 and y_0 are shown in Figs. 9, 10, and 11, respectively.

Figure 9 was obtained with a sensor just beneath the surface at the standard deployment location (at 7.5 m from the tower legs to the southeast), and then at depths of 0.5 and 1.0 m and successively in 1.0-m depth increments, all the way down to a 14.0-m depth. The water column and the atmosphere are assumed homogeneous. In this example, the E_d shadowing increases slightly with depth, the E_u shadowing decreases, and the L_u shadowing remains somewhat constant but with some irregularities.

The effect of realistic media stratification has also been addressed. We modified the standard case at 412 nm by introducing the in-air and in-water particle IOP distributions related to the stratifications described in Subsections 4.A.2 and 4.A.3. The adopted hydrosol IOP values were taken from some typical and moderately stratified WET Labs AC-9 in-water profiles. The results from the study indicate that, for the considered examples, the variability of in-water and above-water IOPs does not strongly influence the shadowing effects, which oscillate by approximately 1% with respect to the results obtained from a standard homogeneous ocean–atmosphere system. The percentage relative errors at the subsurface level (i.e., at 0^--m depth) are listed in Table 5. Note that, for the analyzed cases, atmospheric stratification has the strongest influence on modification of the shadowing results found for the totally homogeneous case, whereas allowance for stratification both in the atmosphere and in the ocean, at least in the case we considered, seems to cancel the shadowing variation.

We obtained Fig. 10 by simulating with the sensor just beneath the surface and by moving it along the x axis on the AAOT deployment platform side, i.e., to the southeast, with variable increments all the way to a distance of 100 m from the tower legs. The results of the shadowing effects on E_d, E_u, and L_u as a function of tower-to-sensor logarithmic on-x-axis distance display a (half) Gaussian-like shape. This feature could be used to parameterize shadowing errors in future developments.

We obtained Fig. 11 with the sensor beneath the surface at the standard deployment location and then by moving it perpendicular to the x axis (i.e., on the y axis) from 0 m with variable increments up to a distance of 10 m, both toward the northeast in positive increments and toward the southeast in negative increments (i.e., left and right with respect to an observer standing on the AAOT deployment platform and looking toward the open sea). The E_d, E_u, and L_u shadowing effects as a function of on-y-axis sensor position also display a Gaussian-like shape of the shadowing profiles, even though it is distorted because of the asymmetry of the in-water illumination that exists across the AAOT deployment platform for a given solar position. In fact, higher shadowing occurs when we move the sensor from the center of the platform to the northeast (i.e., positive direction), where the in-water light field perturbation is higher because of the nearby direct shadow cast by the AAOT deployment platform. Shadowing errors also show that E_u is the quantity most sensitive to sensor location along the y axis, whereas E_d is the least sensitive.

F. $\epsilon_{\Re}$ versus τ_{aer}

The $\epsilon_{\Re}$ values as a function of τ_{aer} are shown in Fig. 12. The standard system is modified to assess the

Table 5. AAOT Tower-Shading Percentage Relative Errors[a]

Media Stratification	ϵ_{E_d}	ϵ_{E_u}	ϵ_{L_u}
No stratification (standard case)	5.25	8.49	6.72
Stratified ocean	5.33	9.05	5.98
Stratified atmosphere	6.65	10.29	8.59
Stratified ocean and atmosphere	5.12	8.31	6.24

[a] ϵ_{E_d}, ϵ_{E_u}, and ϵ_{L_u} on subsurface E_d, E_u, and L_u for the nonstratified standard case and for the added stratified media variations.

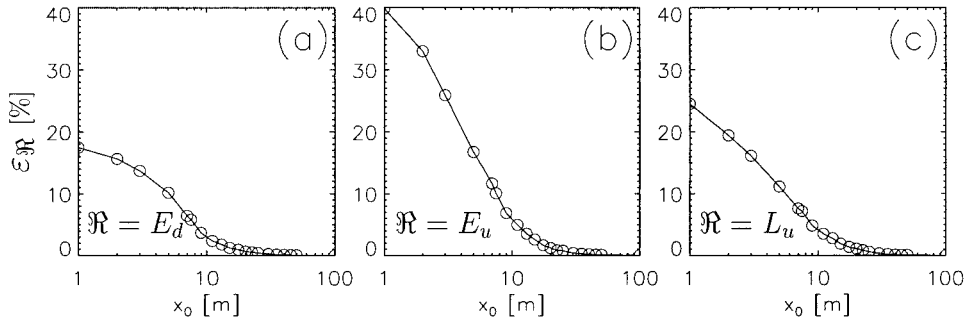

Fig. 10. AAOT tower-shading percentage relative errors (a) ϵ_{E_d}, (b) ϵ_{E_u}, (c) ϵ_{L_u} on subsurface E_d, E_u, and L_u for the standard case as a function of sensor distance along the x axis (x_0 is a component of sensor position X_0).

shadowing effects induced by a wide range of aerosol optical depths. The considered optical depths are $\tau_{\text{aer}} = 0.0$, 0.01, 0.03, 0.10, 0.30, 0.60, and 1.0. Significant influence on shadowing relative errors is observed when we vary τ_{aer} within the chosen range. An increase in aerosol optical depth increases the diffuse illumination regime and consequently increases the portion of skylight (with respect to total light) directly shadowed by the AAOT superstructure. This effect is mostly evident under totally diffuse skylight conditions (i.e., isotropic water-incident photon flux) in which no direct solar light component is present, and the diffuse shadowing accounts for all the shadowing effects that reach values close to 20%.

G. $\epsilon_{\mathcal{R}}$ versus Inherent Optical Properties (in Water)

The $\epsilon_{\mathcal{R}}$ results as a function of a_{hyd} and b_{hyd} are shown in Figs. 13 and 14, respectively. The a_{hyd} hydrosol values are allowed to vary, assuming $a_{\text{hyd}} =$ 0, 0.01, 0.03, 0.10, 0.30, 1.00 m^{-1}. Significant influence on shadowing relative errors is observed when a_{hyd} is varied within the chosen range but, as expected, only for the upwelled quantities because the instrument is at the subsurface level. The observed

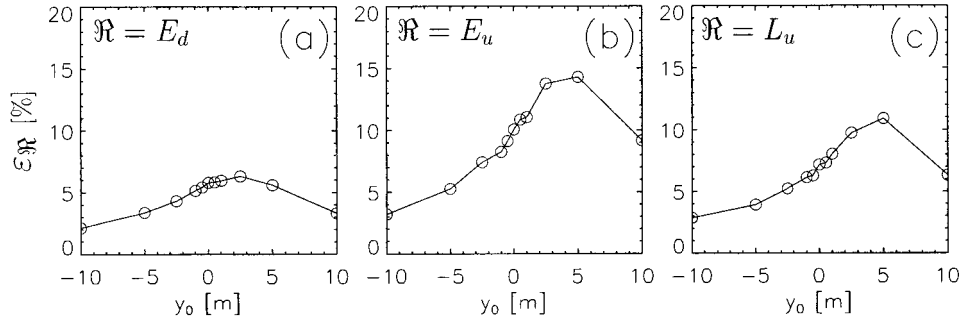

Fig. 11. AAOT tower-shading percentage relative errors (a) ϵ_{E_d}, (b) ϵ_{E_u} (c) ϵ_{L_u} on subsurface E_d, E_u, and L_u for the standard case as a function of sensor distance along the y axis (y_0 is a component of sensor position X_0).

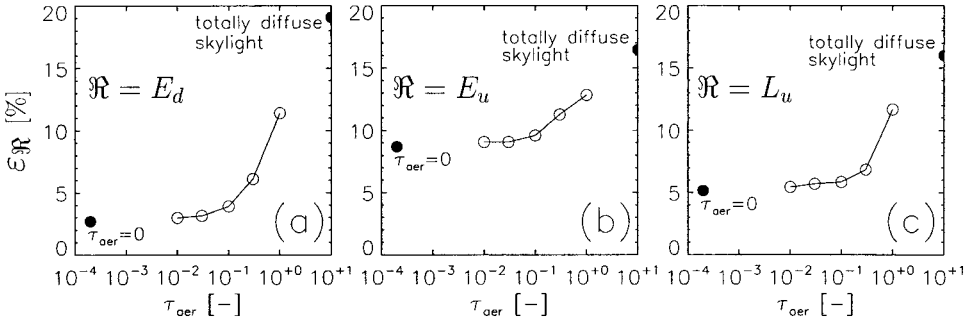

Fig. 12. AAOT tower-shading percentage relative errors (a) ϵ_{E_d}, (b) ϵ_{E_u}, (c) ϵ_{L_u} on subsurface E_d, E_u, and L_u for the standard case as a function of τ_{aer}. The filled circles to the left of the plots represent an atmosphere that contains virtually no aerosol, i.e., $\tau_{\text{aer}} = 0$. The filled circles to the right of the plots represent a totally diffuse above-water illumination (i.e., for an isotropic water-incident photon flux, a condition approached asymptotically when $\tau_{\text{aer}} \rightarrow \infty$).

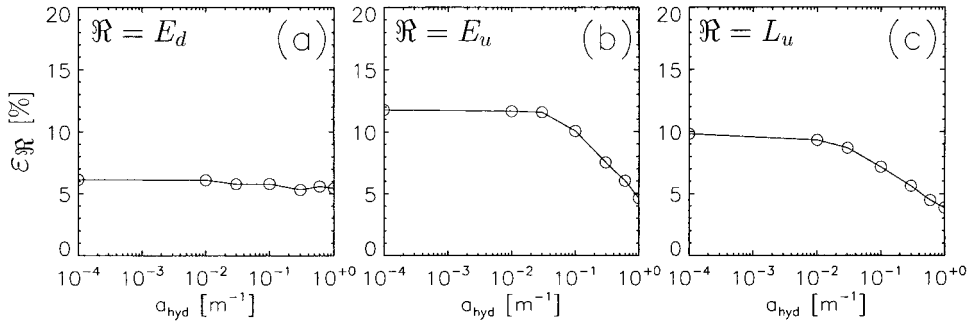

Fig. 13. AAOT tower-shading percentage relative errors (a) ϵ_{E_d}, (b) ϵ_{E_u}, (c) ϵ_{L_u} on subsurface E_d, E_u, and L_u for the standard case as a function of a_{hyd}. The $a_{\mathrm{hyd}} = 0\text{-m}^{-1}$ value corresponds to $a_{\mathrm{hyd}} = 10^{-4}\ \mathrm{m}^{-1}$.

small variations on the subsurface E_d relative error suggest that shadowing occurs only through in-water total internal reflection effects. The upwelled shadowing effects decrease when a_{hyd} increases. In fact, for the given conditions, a higher absorption masks the in-water AAOT shadow as seen by the downlooking subsurface sensor. Specifically, if $a_{\mathrm{hyd}} = 1\ \mathrm{m}^{-1}$, each meter of water decreases, by absorption only, the signal intensity by a factor of e^{-1} (i.e., approximately one third). Then, under these circumstances, a shadow-perturbed water body, sufficiently remote from the sensor (e.g., at 5 m), then barely induces shadowing effects at the sensor location [e.g., $\tilde{\Re} \sim \Re(1 - e^{-5})$].

The b_{hyd} hydrosol values are allowed to vary with respect to the standard system, assuming $b_{\mathrm{hyd}} = 0$, 0.50, 1.00, 2.50, 5.00 m^{-1}. Figure 14 shows only mild shadowing relative errors when we vary b_{hyd}. The exception is L_u, which displays a steep shadowing increase at low b_{hyd}. The general trend—a slight increase in shadowing with an increase in scattering coefficient—is justified by the fact that at low scattering regimes the indirectly propagated shadow (i.e., the signal that never reaches the sensor in the presence of the AAOT structure) is low, although it does increase with multiple scattering effects. L_u undergoes a stronger change in shadowing with respect to E_u, which can be explained by the different FOVs of the L_u and E_u sensors that view different portions of the perturbed field and are affected differently by the scattered light components. However, these dependencies on scattering are also strongly determined by the absolute values of other parameters (such as a_{hyd} and I_r), which significantly influence the overall shadowing effect. Therefore the comments provided for this example are strongly linked to a specific case and are not always applicable to other situations. In general it can be observed that high absorption masks the in-water AAOT shadow, whereas high scattering can fill in the shadow (a same beam attenuation c can produce different shadowing effects, depending on the ω_0 value).

Experimental measurement of the intensity and distribution of in-water scattered light is a demanding effort, so few measurements have been carried out so far. The most widely adopted are the Petzold[36] measurements taken in the San Diego bay. No AAOT *in situ* data has been collected to assess the P_{hyd} properties. A sensitivity study of the AAOT shadowing effects on in-water phase function shape variation would then be ineffective from an operational point of view. However, a simple study has been performed to evaluate the shadowing-error uncertainties associated with the assumption of a specific phase function. We changed the Petzold[36] reference P_{hyd} to Gordon's *KA*[20] in its δ-truncated form,[1] then to a similarly δ-truncated version of the Petzold function, and then to a STHG function with a high forward peak ($g = 0.95$). The results of the shadowing effects on E_d, E_u, and L_u that are due to variable P_{hyd} are shown in Table 6. An appreciable effect can be seen on L_u shadowing, whereas E_d and

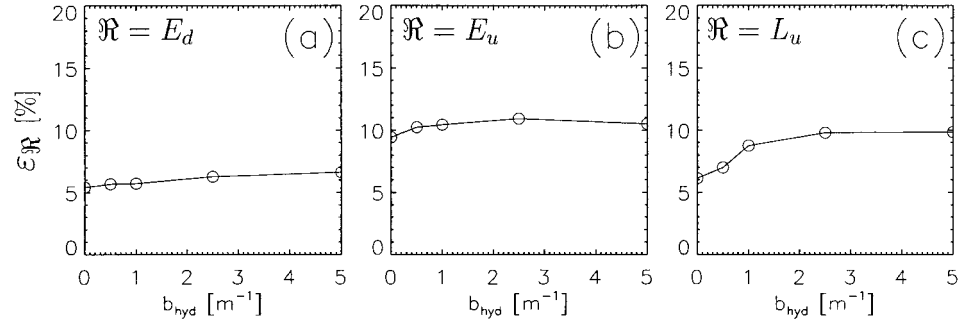

Fig. 14. AAOT tower-shading percentage relative errors (a) ϵ_{E_d}, (b) ϵ_{E_u}, (c) ϵ_{L_u} on subsurface E_d, E_u, and L_u for the standard case as a function of b_{hyd}.

Table 6. AAOT Tower-Shading Percentage Relative Errors[a]

Hydrosol Phase Function P_{hyd}	ϵ_{E_d}	ϵ_{E_u}	ϵ_{L_u}
Petzold (standard case)	5.25	8.49	6.72
Petzold, δ truncated	5.79	10.06	7.16
Gordon's KA', δ truncated	5.59	9.95	6.24
STHG, $g = 0.95$	5.61	10.13	5.50

[a] ϵ_{E_d}, ϵ_{E_u}, and ϵ_{L_u} on subsurface E_d, E_u, and L_u for the standard case, with variable in-water P_{hyd} phase functions added.

E_u shadowing seems less sensitive to a change in P_{hyd}.

6. Shadowing Correction Scheme

We propose a tower-shading correction scheme that relies on MC computations of tower-shading perturbations and is based on the previous sensitivity study. It is intended to be applied to the measurements taken during the widely differing environmental conditions found at the AAOT site. The multidimensional character of the shadowing problem has supported the concept of implementing a look-up table correction scheme, rather than a general analytic approach. The computation of an extensive set of specific correction factors has thus been organized for the construction of look-up tables designed for operational shadow-removal processing. The resulting correction procedure is sufficiently simple that it can be routinely applied to minimize AAOT shadowing perturbations on in-water optical data.

A. Simplified Atmosphere–Ocean System Model

To obtain a practical correction scheme, a simplified and straightforward spectral remodeling of the atmosphere–ocean system has been conducted to reduce the number of system parameters with respect to those that describe the higher dimensioned reference system laid out for the previously described extensive sensitivity study. The simulations were performed at $\lambda = 412, 443, 490, 510, 555, 665$ nm, i.e., the nominal central wavelengths of the *in situ* deployed radiometers that closely match the central wavelengths of the Sea-viewing Wide Field-of-view Sensor (SeaWiFS) instrument.[40]

The atmospheric column is modeled with a single homogeneous layer of depth $D = 60$ km that contains ozone, gas molecules, and aerosol described by their respective beam attenuation coefficients $c_{ozo}(\lambda)$ (mean climatological value from Leckner[41]); $c_{mol}(\lambda)$ (derived by Frölich and Shaw[27] and Young[28] and assigning a fixed $A_p = 1013$ hPa); and $c_{aer}(\lambda)$ [derived from a set of *in situ* realistic $\tau_{aer}(\lambda)$ values]. The Gordon and Castaño[42] marine aerosol P_{aer} was used for the whole spectrum. The water column is also assumed homogeneous, with surface layer IOPs propagated to the sea floor. The $a_{hyd}(\lambda)$ and $c_{hyd}(\lambda)$ coefficients were taken from a discrete set of *in situ* values. A δ-truncated version (following Gordon[1]) of Gordon *et al.*,[20] the *KA* phase function, was assumed for the in-water P_{hyd}. The $\tau_{ozo}(\lambda)$, $\tau_{mol}(\lambda)$, and $r_b(\lambda)$ parameter values are spectrally linked and were fixed to the spectral values assuming, respectively, 300 Dobson units of total atmospheric ozone load, 1013-hPa sea-level atmospheric pressure, and average sea floor reflectance values at the AAOT site.[37] All the other system parameters remained unchanged with respect to the reference system designed for the sensitivity study, including the AAOT 3-D geometry model.

Table 7. Parameters and Their Discretized Values[a]

Parameter	Unit	ind =	1	2	3	4	5	6
$\theta_{0[i]}$	deg		25	30	40	50	60	70
$\phi_{0[j]}$	deg		−135	−90	−45	0	+45	
$\tau_{aer[k]}$	—		0.00	0.05	0.10	0.50	1.00	$\rightarrow\infty$[b]
$a_{[l]}$	m^{-1}		0.02	0.05	0.10	0.30	0.50	
$\omega_{0[m]}$	—		0.50	0.70	0.80	0.85	0.90	0.95

[a] The values were allowed to vary within the simplified atmosphere–ocean system and were used to compute indexed AAOT subsurface tower-shading correction factors $\eta_{\tilde{\Re}}(\lambda)_{[i,j,k,l,m]}$ included in the look-up tables.

[b] The $\rightarrow\infty$ represents the overcast situation and is taken as the limiting parameter value for high ($\gg 1.00$) τ_{aer} values.

B. Shadowing Correction Factor Look-Up Tables

Subsurface tower-shading correction factors $\eta_{\tilde{\Re}}$ ($\eta_{\tilde{E}_d}$, $\eta_{\tilde{E}_u}$, and $\eta_{\tilde{L}_u}$ in separate notation) for the correction of *in situ* perturbed radiometric data $\tilde{\Re}$ are given by the ratio between unperturbed and shadow-perturbed radiometric quantities

$$\eta_{\tilde{\Re}} = \Re/\tilde{\Re} \tag{3}$$

and are estimated through MC simulations designed on the basis of the reduced set of system parameters. The correction of $\tilde{\Re}$ is then simply obtained through multiplication by the adequate $\eta_{\tilde{\Re}}$, which, when we combine Eqs. (1) and (3), is linked to the percentage relative error by $\epsilon_{\Re} = (1 - \eta_{\tilde{\Re}}^{-1}) \times 100$.

For each λ, the $\eta_{\tilde{\Re}}(\lambda)$ factor is computed for a different set of discrete values of the following parameters: θ_0 and ϕ_0 solar angles (allowing also for a θ_0-ϕ_0-independent overcast sky); τ_{aer}, providing a corresponding above surface I_r; total seawater a; total seawater ω_0; and the spectrally linked $r_b(\lambda)$, $\tau_{ozo}(\lambda)$, and $\tau_{mol}(\lambda)$.

Table 7 provides the discretely variable and indexed parameter values θ_0, ϕ_0, τ_{aer}, a, and ω_0 that we used to compute the tower-shading correction factors. Spectral dependence on these parameters has been omitted because, for each λ, all the values of the parameters are distinctly considered to initiate separate correction factor simulations. The discretization range and resolution have been chosen so that they are representative of the variability observed at the AAOT site. Table 8 lists the wavelength-dependent set of values [$r_b(\lambda)$, $\tau_{ozo}(\lambda)$, $\tau_{mol}(\lambda)$].

The correction factors $\eta_{\tilde{\Re}}(\lambda)$ are pointed at by use of indices $[i, j, k, l, m]$ associated with the generating parameters from Table 7 and spectrally grouped as discrete values within a look-up table. Each parameter index (ind ≡ i, j, k, l, m) varies from 1 to 6 at

Table 8. Spectrally Linked Parameters (All Dimensionless)[a]

Parameter	λ =	412 nm	443 nm	490 nm	510 nm	555 nm	665 nm
$r_b(\lambda)$		1.3×10^{-2}	1.8×10^{-2}	3.1×10^{-2}	4.0×10^{-2}	6.1×10^{-2}	26.6×10^{-2}
$\tau_{ozo}(\lambda)$		6.6×10^{-4}	1.0×10^{-3}	7.4×10^{-3}	1.4×10^{-2}	3.3×10^{-2}	1.7×10^{-2}
$\tau_{mol}(\lambda)$		0.32	0.24	0.16	0.13	0.09	0.04

[a]Their spectrally fixed values were allowed to covary with λ within the simplified atmosphere–ocean system and were used to compute AAOT tower-shading correction factors included in the look-up tables.

most. We obtained the $\eta_{\tilde{\Re}}(\lambda)_{[i,j,k,l,m]}$ correction factors by performing a total of approximately 100,000 independent backward MC simulations each supported by 10^5–10^7 primary photons.

The appropriate correction factor $\eta_{\tilde{\Re}}$ for an actual subsurface radiometric measurement is found through a matching of the actual parameter values across the parameter grid that underlies the look-up table, with the exception of τ_{aer} for which we substituted I_r as a result of our computations. The range of variability in I_r has in fact been reproduced by simulation of the tower-shading errors in clear-sky conditions with different values for τ_{aer}, where $\tau_{aer} = c_{aer}D$. A suggested improvement in the current use of the look-up tables is to operate appropriate parameter–correction-factor interpolations rather than to seek a match.

Even though the proposed look-up tables are valid in principle only under clear-sky conditions, the use of I_r (instead of τ_{aer}) as a matching parameter for indexed $\eta_{\tilde{\Re}}$ values has been suggested by the need to refer to a quantity that is capable of describing general illumination conditions in an integrated way, also accounting for skylight distribution inhomogeneities (e.g., induced by the presence of clouds). In fact, under the latter circumstances, the simple τ_{aer} (obtained along the solar direction) can be less representative than I_r of the actual field measurement conditions. Appropriate $\eta_{\tilde{\Re}}$ correction factors are also provided for totally diffuse skylight, assuming an

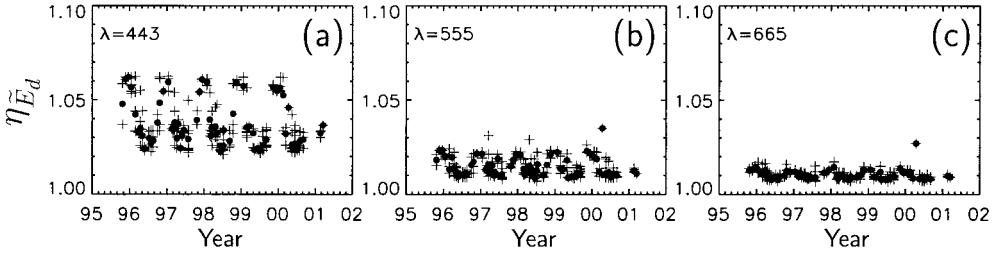

Fig. 15. AAOT $\eta_{\tilde{\Re}}(\lambda)$ correction factors as a function of sampling time (between October 1995 and February 2001) for the shadowed subsurface downwelling irradiance $\tilde{E}_d$ at λ = (a) 443, (b) 555, (c) 665 nm. The dots represent average campaign values, crosses indicate single measurement values (a single campaign can include as much as one week of data).

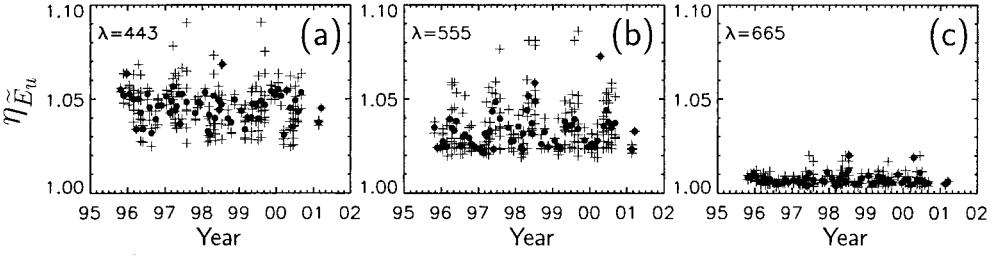

Fig. 16. As in Fig. 15 but for $\eta_{\tilde{E}_u}(\lambda)$.

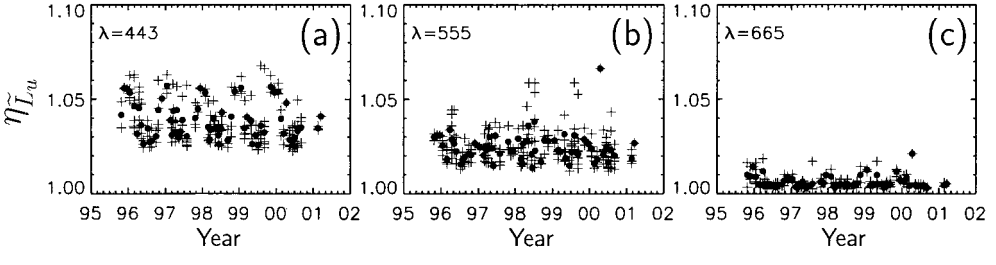

Fig. 17. As in Fig. 15 but for $\eta_{\tilde{L}_u}(\lambda)$.

Table 9. Average and Standard Deviation of Subsurface Tower-Shadowing Percentage Relative Errors[a]

Parameter	Unit	412 nm	443 nm	490 nm	510 nm	555 nm	665 nm
$\epsilon_{\tilde{E}_d}$	—	4.37 [1.42]	3.49 [1.19]	2.43 [0.86]	2.06 [0.73]	1.40 [0.50]	0.98 [0.22]
$\epsilon_{\tilde{E}_u}$	—	4.58 [1.05]	4.32 [1.03]	4.14 [1.03]	3.76 [1.07]	3.20 [1.13]	0.71 [0.34]
$\epsilon_{\tilde{L}_u}$	—	4.28 [1.31]	3.67 [1.04]	3.19 [1.04]	2.87 [0.87]	2.35 [0.77]	0.55 [0.30]
a_{hyd}	m^{-1}	0.217 [0.084]	0.100 [0.066]	0.098 [0.036]	0.067 [0.026]	0.037 [0.014]	0.032 [0.028]
w_0	—	0.795 [0.069]	0.823 [0.066]	0.858 [0.055]	0.856 [0.060]	0.847 [0.068]	0.508 [0.162]
I_r	—	0.844 [0.369]	0.671 [0.307]	0.499 [0.254]	0.438 [0.247]	0.336 [0.186]	0.223 [0.148]

[a] $\epsilon_{\Re}$ values for $\tilde{E}_d$, $\tilde{E}_u$, and $\tilde{L}_u$ AAOT data, and the average and standard deviation of the relevant parameters used to retrieve the subsurface $\eta_{\tilde{\Re}}$ values from the look-up tables. Measurements were taken with solar zenith θ_0 varying between 22° and 77° (48° average), and compass solar azimuth ϕ_0' varying between 87° and 245° (163° average). The numbers within brackets represent the standard deviation.

isotropic above-water incident photon distribution. This situation is taken to represent the limiting illumination case when $I_r \rightarrow \infty$ (when $\tau_{\mathrm{aer}} \rightarrow \infty$).

The $\eta_{\tilde{\Re}}$ correction factors, extracted from look-up tables for correction of 360 actual WiSPER measurements taken under clear-sky conditions, are plotted as a function of time for the period from October 1995 to February 2001 at the three representative wavelengths of 443, 555, and 665 nm. The correction factors displayed in Figs. 15, 16, and 17 for subsurface $\tilde{E}_d$, $\tilde{E}_u$, and $\tilde{L}_u$, respectively, are given for each measurement (crosses) and as campaign averages (circles). All $\eta_{\tilde{\Re}}$ correction factors show the lowest values, generally less than 1.02, at 665 nm and the highest values, generally between 1.02 and 1.09, at 443 nm. The $\eta_{\tilde{E}_d}$ and $\eta_{\tilde{L}_u}$, and also to some extent $\eta_{\tilde{E}_u}$, mean values at 443 nm display a clear seasonal pattern with the highest values in winter and the lowest values in summer. This can be explained mostly by the solar zenith variations across the year. In fact, most of the WiSPER measurements were taken around local noon when solar zenith has the lowest daily values. The variability that overlaps the seasonal cycle can be explained by changes in seawater and atmospheric optical properties and by daily changes in solar zenith. Table 9 shows the average and standard deviation of the percentage error values $\epsilon_{\Re}$ that affect the WiSPER $\tilde{E}_d$, $\tilde{E}_u$, and $\tilde{L}_u$ data. In addition, the average and standard deviations of the relevant parameters used to retrieve $\eta_{\tilde{\Re}}$ from the look-up tables are also given.

Major limitations in the correction scheme proposed for AAOT tower-shading effects on the collected radiometry when roughness is neglected in modeling sea surface reflectance; assuming that the tower structure absorbs all the incident photons (i.e., not reflecting); using correction factors computed for discrete values of the input variables θ_0, ϕ_0, τ_{aer}, a, and ω_0; and assuming homogeneous water column IOPs.

These limitations notwithstanding, the correction scheme is now implemented in an optical data-processing system to be routinely used within the framework of long-term time-series measurement activities for operational correction of tower-shading effects in optical data acquired at the AAOT site.

7. Conclusions

The use of backward MC methods allows realistic shadowing effects that occur on *in situ* underwater radiance and irradiance measurements to be simulated accurately. In particular, complex geometry oceanographic towers can be effectively modeled, and their shadowing effects can be accounted for and corrected for. For this study we conducted MC simulations on a model of the northern Adriatic Sea AAOT platform by applying a completely 3-D backward MC code (PHO-TRAN) developed by one of the authors.[12] We validated the code extensively against literature data, taking into account complex 3-D geometries and variable IOPs associated with natural media. The environmental conditions that were retained for modeling purposes comprise an evenly distributed collection of conditions normally found at the investigated oceanographic site. These conditions take into account the illumination geometry, the atmospheric composition together with its structure and optical properties, the air–sea interface characteristics, the oceanic composition together with its structure and optical properties, the sea floor characteristics, the deployment structure geometry and optical characteristics, and the light collection design characteristics of the detectors.

By making use of the MC code, we investigated and substantiated the specific AAOT perturbation effects extensively by conducting a sensitivity study that showed that the tower-shading errors on E_d, E_u, and L_u are particularly sensitive to change in θ_0, ϕ_0, λ, X_0, τ_{aer}, a_{hyd}, and, to a lesser extent, in b_{hyd}. For an analyzed homogeneous water-column case study, the sensitivity of the response to detector depth has been shown to be marginal, with the exception of perturbations on E_u. This, together with the study carried out for a stratified atmosphere–ocean system, allows application of, to within a few percent accuracy, subsurface shadow-correction factors to optical data at different depths along a homogeneous water column (even though care is suggested when parameter values significantly depart from those assigned in the considered case study). The sensitivity analysis has enabled the appropriate selection of values and ranges of optical, geometric, and environmental pa-

rameters to be used in the computation of extensive sets of tower-shading correction factors for routine radiance and irradiance measurements taken at the AAOT site. The correction factors have been grouped in look-up tables indexed through relevant optical and geometric parameter values. The proposed correction scheme has been shown to be efficient for the removal of tower-shading perturbations that occur on in-water radiometric AAOT data acquired within the framework of the Coastal Atmosphere and Sea Time-Series (CoASTS) project.[37] Tower-shading correction factors estimated with the proposed methodology for E_d, E_u, and L_u measurements taken at the AAOT site between October 1995 and February 2001 under clear-sky conditions have shown values less than 1.02 at 665 nm and ranging from 1.02 up to 1.09 at 443 nm. The latter correction values can rise up to 1.20 under extreme but realistic conditions (i.e., overcast sky or clear sky with high Sun zenith angles). A first experimental assessment of the former correction values has been attempted with field data.[7] Results support the validation of the applied MC simulation technique, even though we believe that a more extensive assessment would add additional consistency and reliability to the correction scheme.

The significant uncertainties induced in optical measurements taken at the AAOT site sustain the more general need to minimize deployment structure perturbations in optical measurements collected in the vicinity of towers, ships, or buoys to ensure high accuracy of data for bio-optical modeling, to validate remote-sensing products, and for vicarious calibration of space sensors. The proposed correction methodology, although developed for the parameters that characterize the AAOT site, can be, in principle, transferred to other systems if their correct 3-D description is given together with the full range of environmental and optical parameters that are representative of the specific site being investigated. This would allow us to handle the correction of shadowed data acquired from other deployment structures and detected within varied instrument casings and package geometries, in markedly different waters, and under complex illumination conditions. Nonetheless, the most accurate and flexible use of MC simulations is to perform quasi-real-time computations for each individual measurement, having comprehensively and simultaneously characterized the underlying Sun–atmosphere–ocean–structure–detector system. This more flexible approach is particularly advisable when tower-shading effects must be estimated at depth and for stratified media.

Appendix A: Variance Reduction Techniques

The photon backtracking scheme described in Subsection 2.B is straightforward, however, it can be computationally inefficient. To waste less photons and thus decrease both computational time and statistical variance on the computed quantities, some variance-reducing techniques have been implemented in the computational procedures developed for the PHO-TRAN MC code.

Statistical variance is reduced by use of deterministic techniques and by extraction of as much weight as possible from the photon's history, as uniformly as possible over history space. Each time a photon weight is multiplied by a given interaction probability coefficient (i.e., cross section), variance reduction is obtained. The photon is in fact more rigorously defined as a photon probabilistic weight, which is linked to the proportion of actual surviving photons (i.e., the ratio between the number of photons that exit a radiation–matter interaction and those that enter the process). In each of the following subsections a distinct variance-reducing technique is introduced.

1. Virtual Photons

Strictly speaking, the use of virtual photons as defined previously is itself a variance-reduction technique, not dissimilar to the point detector[16] variance-reduction scheme. Point detectors are obtained by analytic propagation of radiation from collision events to detector location. This might not be the most probable photon ray, but it is a surely detected one, and its contribution to the detected signal is generally highly efficient, thus reducing the associated variance.

2. Semi-Systematic Sampling

The backward emitted photon polar direction is sampled according to a semi-systematic sampling scheme.[16] This means that random selection of polar angles is restricted to angular bins from which sampling has not yet occurred, thereby allowing a more uniform selection of random directions. This variance-reduction technique does not force polar angles to fixed binned values, so any unwanted directional discretization is avoided. The same scheme is also applied for the selection of polar scattering angles from an equal probability tabulated scattering CDF, where each equal probability interval is semi-systematically sampled.

3. Forced Absorption

The absorption event following a collision is modified. Instead of losing a photon in an absorption process and therefore wasting its potential for further deterministic contributions, one can decrease the photon weight by multiplying its value by the photon's interaction survival probability (i.e., the ω_{tot} value of the material that fills the cell that contains the collision point). The photon is then forced to scatter, according to one of the possible scattering mechanisms. The same principle is applied to photon collision on a (partially) absorbing interface (e.g., a surface).

4. Forced Collisions

The optical distance to the next collision is sampled according to whether the extrapolated backward photon path leaks, i.e., crosses one of the boundaries that enclose the modeled system (such as the TOA plane

or the vertical sides of the large rectangular box that globally encloses the modeled atmosphere–ocean system). If the extrapolated path crosses such a boundary, we reduce the variance by sampling the optical path to the next collision by using a truncated exponential distribution rather than a simple exponential distribution, i.e., the sampling scheme adopted for nonleaking extrapolated backward photon paths. The truncation forces the photon to collide before it reaches the boundary, thus avoiding photon leakage. Forced collisions are imposed by sampling the photon's free-flight optical path τ_f according to $p_{esc}(\tau_f)$, a PDF given by the product of a classical exponential PDF multiplied by a truncating factor

$$p_{esc}(\tau_f) = \exp(-\tau_f)[1 - \exp(-\tau_{esc})]^{-1}, \quad \text{(A1)}$$

where $0 \leq \tau_f \leq \tau_{esc}$. To remove the bias introduced by the technique, the photon weight at this forced collision point is multiplied by an appropriate factor $[1 - \exp(-\tau_{esc})]$. The latter is equal to the probability of the photon to escape from the system that travels the full optical path, τ_{esc}, separating it from the leakage boundary. Whether collisions are forced or not, the semi-systematic sampling technique described above is also used to select the appropriate free-flight optical distance bin. Again, this does not introduce discretization in the actual sampled distances, because they are allowed to vary with continuity within a bin.

5. Stacked Reflections

At an interface between media of different refractive indices, rather than choosing a random number to determine whether a photon is transmitted or reflected, we reduce variance by allowing both events to occur. A photon reflected by an interface is stacked, and its set of characteristic parameter values (x, y, z, θ, ϕ, W, and the optical paths τ_p or τ_f remaining prior to collision) are later retrieved for further tracking after the history of the transmitted photon is exhausted (this does not occur for total internal reflection).

6. δ Truncation

Diffraction peak truncation or δ truncation[43,44] of the scattering phase functions for aerosol or in-water particulate matter can be adopted to decrease variance in the backtracking and sampling schemes and thus to increase the simulation's statistical precision at the expense of accuracy in the description of effects that are due to a high forward-scattering peak at very small ($< 7°$) positive angles. Details of the truncation scheme are given by Gordon.[1]

7. Russian Roulette

The application of variance-reduction schemes reduces the weight of randomly tracked photons. Their importance is also reduced owing to exponential decay, when transmission occurs across attenuating media, and to abrupt stepwise reduction when the photons cross imperfectly transmitting interfaces. A randomly tracked photon is terminated when its weight W falls below a predetermined threshold value $\bar{W}$, typically 10^{-6}, which can occur rapidly in strongly absorbing media or can take a long time in highly scattering mixtures. To ensure statistical coherence within MC results for different systems, the threshold value is precomputed according to Morel and Gentili,[45] so that, on average, a comparable number of collisions occurs within a given distance from the detector (computed by use of the average ω_{tot}). The number of initiated photons (of the order of 10^5–10^6) affects the estimated SRE, i.e., the estimated standard deviation of the mean divided by the estimated mean, obtained for simulated data. The SRE has been maintained below 0.01 for all the simulations performed to assess tower-shading effects. When the decreased photon weight W falls below the predetermined cutoff threshold, rather than invariably terminating its history, we determine the photon's life by the technique of Russian Roulette. This is a variance-reducing technique that either resets the photon weight back to its initial unitary value, with a probability equal to its currently achieved low weight, or otherwise terminates the photon's history. A random number $u \in U[0, 1]$ is sampled: if $u \leq \bar{W}$ then $W = W_0$, otherwise the photon is killed ($W = 0$) and removed from the MC game. No bias is introduced by Russian Roulette.[10]

8. Correlated Sampling

Correlated sampling is a powerful variance-reducing technique that is used to distinguish between small differences of estimated quantities. We produced the latter small differences by introducing a structural parameter perturbation into the system. By tracking so-called twin photons, one interacting with the intervening structure and the other not, one can achieve a correlated sampling scheme.[10] This minimizes the score variance of differences between signals carried from photons transported in the perturbed and unperturbed systems. If f and f' are, respectively, unperturbed and perturbed MC estimated mean responses obtained for a corresponding change $\Delta\wp = \wp - \wp'$ in system parameter $\wp$ (where, for example, $\wp = \omega_{tot}$ and $\wp'$ is its perturbed counterpart, $\wp' = \omega_{tot}' \equiv 0$), then the variance in the difference $\Delta f = f - f'$ is given by[10]

$$\mathrm{var}(\Delta f) = \mathrm{var}(f) + \mathrm{var}(f') - 2\,\mathrm{cov}(f, f'), \quad \text{(A2)}$$

where $\mathrm{var}(f)$ is the variance of the estimated quantity f, and $\mathrm{cov}(f, f')$ is the covariance of f and f'. When the two estimates are obtained by two independent MC runs, the correlation term $2\,\mathrm{cov}(f, f')$ of Eq. (A2) vanishes because f and f' are completely uncorrelated. Then $\mathrm{var}(\Delta f)$ is just the sum of $\mathrm{var}(f)$ and $\mathrm{var}(f')$:

$$\mathrm{var}(\Delta f) = \mathrm{var}(f) + \mathrm{var}(f'). \quad \text{(A3)}$$

For small $\Delta\wp$ the estimate Δf is usually given through the relative change $\Delta f/\Delta\wp$. As the sum in Eq. (A3) is

positive and finite, for small $\Delta\wp$ the relative variance can increase without limit

$$\lim_{\Delta\wp\to 0} \mathrm{var}(\Delta f/\Delta\wp) = \frac{\mathrm{var}(f) + \mathrm{var}(f')}{\Delta\wp^2} \to \infty. \quad \text{(A4)}$$

On the other hand, if it is possible to correlate the calculation of the expectations of f and f', then, according to Rief,[46] the relative variance could assume a finite value:

$$\lim_{\Delta\wp\to 0} \mathrm{var}(\Delta f/\Delta\wp) = \frac{\mathrm{var}(f) + \mathrm{var}(f') - 2\ \mathrm{cov}(f, f')}{\Delta\wp^2} \to \kappa < \infty, \quad \text{(A5)}$$

where κ is a constant. If f and f' are strongly correlated, as happens when MC estimates are carried out by use of the same set of random numbers and to the extent that Δf is small, then[1]

$$2\ \mathrm{cov}(f, f') \simeq \mathrm{var}(f) + \mathrm{var}(f'), \quad \text{(A6)}$$

thus [from Eq. (A5)] $\kappa \simeq 0$, and the variance in Δf is reduced to less than that of either f or f'.

All the variance-reduction schemes described previously increase the efficiency and the precision of the MC computations, whereas the relative accuracy is generally maintained to within 0.01% with respect to the analog MC simulations (i.e., those performed without the use of variance-reduction techniques).

This research has been supported in part by the European Commission within the Marine Science and Technology project COLORS. Davide D'Alimonte is duly acknowledged for providing software to display correction factors from the look-up tables database. Valuable oceanic and atmospheric modeling recommendations have been provided by Barbara Bulgarelli and Jean-François Berthon. Computation of look-up table factors was made possible thanks to the experimental data provided by Jean-François Berthon (WET Labs AC-9 *in situ* seawater absorption and beam attenuation coefficients) and by Stefania Grossi (Perkin-Elmer Lambda *in vivo* aquatic particulate and colored dissolved organic matter absorption coefficients). We are grateful to H. R. Gordon for granting us permission to reproduce some of his previously published data.

References

1. H. R. Gordon, "Ship perturbation of irradiance measurements at sea. 1. Monte Carlo simulations," Appl. Opt. **24,** 4172–4182 (1985).
2. K. J. Voss, J. W. Nolten, and G. D. Edwards, "Ship shadow effects on apparent optical properties," in *Ocean Optics VIII*, M. A. Blizard, ed., Proc. SPIE **637,** 186–190 (1986).
3. W. S. Helliwell, G. N. Sullivan, B. MacDonald, and K. J. Voss, "Ship shadowing: model and data comparisons," in *Ocean Optics X*, R. W. Spinrad, ed., Proc. SPIE **1302,** 55–71 (1990).
4. C. T. Weir, D. A. Siegel, A. F. Michaels, and D. W. Menzies, "*In situ* evaluation of a ship's shadow," in *Ocean Optics XII*, J. S. Jaffe, ed., Proc. SPIE **2258,** 815–821 (1994).
5. E. Kearns, R. Riley, and C. Woody, "Bio-optical time series collected in coastal waters for SeaWiFS calibration and validation: large structure shadowing considerations," in *Ocean Optics XIII*, S. G. Ackleson, ed., Proc. SPIE **2963,** 697–702 (1996).
6. Y. Saruya, T. Oishi, M. Kishino, Y. Jodai, K. Kadokura, and A. Tanaka, "Influence of ship shadow on underwater irradiance fields," in *Ocean Optics XIII*, S. G. Ackleson, ed., Proc. SPIE **2963,** 760–765 (1996).
7. G. Zibordi, J. P. Doyle, and S. B. Hooker, "Offshore tower shading effects on in-water optical measurements," J. Atmos. Oceanic Technol. **16,** 1767–1779 (1999).
8. J. L. Mueller and R. W. Austin, "Ocean optics protocols for SeaWiFS validation, revision 1," *SeaWiFS Project Technical Report Series*, NASA Tech. Memo. 104566, Vol. 25, S. B. Hooker, E. R. Firestone, and J. G. Acker, eds. (NASA Goddard Space Flight Center, Greenbelt, Md., 1995).
9. H. R. Gordon and K. Ding, "Self-shading of in-water optical instruments," Limnol. Oceanogr. **37,** 491–500 (1992).
10. J. Spanier and E. M. Gelbard, *Monte Carlo Principles and Neutron Transport Problems* (Addison-Wesley, Reading, Mass., 1969).
11. J. P. Doyle and H. Rief, "Photon transport in three-dimensional structures treated by random walk techniques: Monte Carlo benchmark of ocean colour simulations," Math. Comput. Simul. **47,** 215–241 (1998).
12. J. P. Doyle is preparing a Ph.D. dissertation called "Monte Carlo modelling of radiative transfer in a 3-D ocean–atmosphere system: ocean colour simulations," (Imperial College of Science, Technology, and Medicine, University of London, London, UK, 2002).
13. E. D. Cashwell and C. J. Everett, *Practical Manual on the Monte Carlo Method for Random Walk Problems* (Pergamon, New York, 1959).
14. C. Cox and W. Munk, "Slopes of the sea surface deduced from photographs of Sun glitter," Scripps Inst. Oceanogr. Bull. **6,** 401–488 (1956).
15. K. M. Case, "Transfer problems and the reciprocity principle," Rev. Mod. Phys. **29,** 651–663 (1957).
16. I. Lux and L. Koblinger, *Monte Carlo Transport Methods; Neutron and Photon Calculations* (CRC Press, Boca Raton, Fla., 1991).
17. C. D. Mobley, *Light and Water: Radiative Transfer in Natural Waters* (Academic, San Diego, Calif., 1994).
18. C. D. Mobley, B. Gentili, H. R. Gordon, Z. Jin, G. W. Kattawar, A. Morel, P. Reinersman, K. Stamnes, and R. H. Stavn, "Comparison of numerical models for computing underwater light fields," Appl. Opt. **32,** 7484–7504 (1993).
19. B. Bulgarelli, V. Kisselev, and L. Roberti, "Radiative transfer in the atmosphere–ocean system: the finite-element method," Appl. Opt. **38,** 1530–1542 (1999).
20. H. R. Gordon, O. B. Brown, and M. M. Jacobs, "Computed relationships between the inherent and apparent optical properties of a flat homogeneous ocean," Appl. Opt. **14,** 417–427 (1975).
21. J. F. Berthon, G. Zibordi, J. P. Doyle, S. Grossi, D. van der Linde, and C. Targa, "Coastal Atmosphere and Sea Time Series (CoASTS). Part 2: Data analysis," in *SeaWiFS Project Technical Report Series*, NASA Tech. Memo. TM-2002-206892 **20,** S. B. Hooker and E. R. Firestone, eds. (NASA Goddard Space Flight Center, Greenbelt, Md., 2002).
22. G. Zibordi and M. Ferrari, "Instrument self-shading in underwater optical measurements: experimental data," Appl. Opt. **34,** 2750–2754 (1995).
23. H. Neckel and D. Labs, "The solar radiation between 3300 and 12500 Å," Sol. Phys. **90,** 205–258 (1984).
24. A. A. Lacis and J. E. Hansen, "Parameterization for the absorption of solar radiation in the Earth's atmosphere," J. Atmos. Sci. **31,** 118–133 (1974).

25. E. Vigroux, "Contribution a l'etude experimentale de l'absorption de l'ozone," Ann. Phys. **8,** 709–762 (1953).
26. W. A. Margraaf and M. Griggs, "Aircraft measurements and calculations of the total downward flux of the solar radiation as a function of altitude," J. Atmos. Sci. **26,** 469–477 (1969).
27. C. Frölich and G. E. Shaw, "New determination of Rayleigh scattering in the terrestrial atmosphere," Appl. Opt. **19,** 1773–1775 (1980).
28. A. T. Young, "Revised depolarization corrections for atmospheric extinction," Appl. Opt. **19,** 3427–3428 (1980).
29. A. Ångström, "Techniques of determining the turbidity of the atmosphere," Tellus **13,** 214–223 (1969).
30. L. Elterman, "UV, visible and IR attenuation for altitudes to 50 km," Environmental Research Papers 285, AFCRL-68-0153 (U.S. Air Force Cambridge Research Laboratories, L. G. Hanscom Field, Bedford, Mass., 1968).
31. L. C. Henyey and J. L. Greenstein, "Diffuse radiation in the galaxy," Astrophys. J. **93,** 70–83 (1941).
32. B. Sturm and G. Zibordi, "SeaWiFS atmospheric correction by an approximate model and vicarious calibration," Int. J. Remote Sens. **23,** 489–501 (2002).
33. R. M. Pope and E. S. Fry, "Absorption spectrum (380–700 nm) of pure water. II. Integrating cavity measurements," Appl. Opt. **36,** 8710–8723 (1997).
34. H. Buiteveldt, J. H. M. Hakvoort, and M. Donze, "Optical properties of pure water," in *Ocean Optics XII*, J. S. Jaffe, ed., Proc. SPIE **2258,** 174–183 (1994).
35. A. Morel, "Optical properties of pure water and pure seawater," in *Optical Aspects of Oceanography*, N. G. Jerlov and E. S. Nielsen, eds. (Academic, New York, 1974), pp. 1–24.
36. T. J. Petzold, "Volume scattering functions for selected natural waters," SIO Ref. 72-78 (Visibility Laboratory, Scripps Institution of Oceanography, University of California, San Diego, La Jolla, Calif., 1972).
37. G. Zibordi, J. F. Berthon, J. P. Doyle, S. Grossi, D. van der Linde, C. Targa, and L. Alberotanza, "Coastal Atmosphere and Sea Time Series (CoASTS). Part 1: A long-term measurement program," in *SeaWiFS Project Technical Report Series*, NASA Tech. Memo. TM-2002-206892 **19,** S. B. Hooker and E. R. Firestone, eds. (NASA Goddard Space Flight Center, Greenbelt, Md., 2002).
38. Lord Rayleigh, "On the light from the sky, its polarization and colour," Philos. Mag. **41,** 107–120, (1871), reprinted in *Scientific Papers by Lord Rayleigh, Vol I: 1869–1881* (Dover, New York, 1964).
39. A. Einstein, "Theorie der Opaleszenz von homogenen Flüssigkeiten und Flüssigkeitsgemischen in der Nähe des kritischen Zustandes," ("Theoretical aspects of the opalescence of homogeneous fluids and liquid mixtures near the critical state"), Ann. Phys. (Leipzig) **33,** 1275–1298 (1910).
40. S. B. Hooker and C. R. McClain, "The calibration and validation of SeaWiFS data," Prog. Oceanogr. **45,** 427–465 (2000).
41. B. Leckner, "The spectral distribution of solar radiation at the Earth's surface: elements of a model," Sol. Energy **20,** 143–150 (1978).
42. H. R. Gordon and D. J. Castaño, "The Coastal Zone Color Scanner atmospheric correction algorithm: multiple scattering effects," Appl. Opt. **26,** 2111–2122 (1987).
43. J. F. Potter, "The delta function approximation in radiative transfer theory," J. Atmos. Sci. **27,** 943–949 (1969).
44. M. Tanaka and T. Nakajima, "Effects of oceanic turbidity and index of refraction of hydrosols on the flux of solar radiation in the atmosphere–ocean system," J. Quant. Spectrosc. Radiat. Transfer **18,** 93–111 (1977).
45. A. Morel and B. Gentili, "Diffuse reflectance of oceanic waters: its dependence on Sun angle as influenced by the molecular scattering contribution," Appl. Opt. **30,** 4427–4438 (1991).
46. H. Rief, "Stochastic perturbation analysis applied to neutral particle transport," Adv. Nucl. Sci. Technol. **23,** 69–140 (1996).